Geoscience Frontiers 10 (2019) 2021–2044

HOSTED BY

ELSEVIER

Contents lists available at ScienceDirect

China University of Geosciences (Beijing)

Geoscience Frontiers

journal homepage: www.elsevier.com/locate/gsf

Research Paper

Petrology, geochemistry, and zircon U-Pb geochronology of the Zambezi Belt in Zimbabwe: Implications for terrane assembly in southern Africa

Yusuke Kuribara [a], Toshiaki Tsunogae [a,b,*], Yusuke Takamura [a], Yukiyasu Tsutsumi [c]

[a] Graduate School of Life and Environmental Sciences, University of Tsukuba, Ibaraki 305-8572, Japan
[b] Department of Geology, University of Johannesburg, Auckland Park 2006, South Africa
[c] Department of Geology and Paleontology, National Museum of Nature and Science, Ibaraki 305-0005, Japan

ARTICLE INFO

Article history:
Received 3 October 2017
Received in revised form
17 February 2018
Accepted 27 May 2018
Available online 2 August 2018

Keywords:
Geothermobarometry
Detrital zircon
Neoproterozoic
Congo Craton
Kalahari Craton
Gondwana

ABSTRACT

The Zambezi Belt in southern Africa has been regarded as a part of the 570–530 Ma Kuunga Orogen formed by a series of collision of Archean cratons and Proterozoic orogenic belts. Here, we report new petrological, geochemical, and zircon U-Pb geochronological data of various metamorphic rocks (felsic to mafic orthogneiss, pelitic schist, and felsic paragneiss) from the Zambezi Belt in northeastern Zimbabwe, and evaluate the timing and *P-T* conditions of the collisional event as well as protolith formation. Geochemical data of felsic orthogneiss indicate within-plate granite signature, whereas those of mafic orthogneiss suggest MORB, ocean-island, or within-plate affinities. Metamorphic *P-T* estimates for orthogneisses indicate significant *P-T* variation within the study area (700–780 °C/6.7–7.2 kbar to 800–875 °C/10–11 kbar) suggesting that the Zambezi Belt might correspond to a suture zone with several discrete crustal blocks. Zircon cores from felsic orthogneisses yielded two magmatic ages: 2655 ± 21 Ma and 813 ± 5 Ma, which suggests Neoarchean and Early Neoproterozoic crustal growth related to within-plate magmatism. Detrital zircons from metasediments display various ages from Neoarchean to Neoproterozoic (ca. 2700–750 Ma). The Neoarchean (ca. 2700–2630 Ma) and Paleoproterozoic (ca. 2200–1700 Ma) zircons could have been derived from the adjacent Kalahari Craton and the Magondi Belt in Zimbabwe, respectively. The Choma-Kalomo Block and the Lufilian Belt in Zambia might be proximal sources of the Meso- to Neoproterozoic (ca. 1500–950 Ma) and early Neoproterozoic (ca. 900–750 Ma) detrital zircons, respectively. Such detrital zircons from adjacent terranes possibly deposited during late Neoproterozoic (744–670 Ma), and subsequently underwent high-grade metamorphism at 557–555 Ma possibly related to the collision of the Congo and Kalahari Cratons during the latest Neoproterozoic to Cambrian. In contrast, 670–627 Ma metamorphic ages obtained from metasediments are slightly older than previous reports, but consistent with ~680–650 Ma metamorphic ages reported from different parts of the Kuunga Orogen, suggesting Cryogenian thermal events before the final collision.

1. Introduction

Recent geological, petrological, and geochronological studies on Late Neoproterozoic to Cambrian orogenic belts from different regions in the world indicate that the Gondwana Supercontinent was not formed by a simple collision of East and West Gondwana continents, but was established by a series of continent-continent, arc-continent, and arc-arc collisions between 750 Ma and 530 Ma (e.g., Meert and Voo, 1997; Meert, 2003; Jacobs and Thomas, 2004; Collins and Pisarevsky, 2005; Collins et al., 2007a,b; Meert and Lieberman, 2008; Santosh et al., 2009a). Particularly, many recent studies on high-grade metamorphic rocks from southern India, Sri Lanka, Madagascar, and East Antarctica regions in East Gondwana have focused on unraveling the structural and metamorphic processes in these regions, as the juxtaposition of these crustal blocks is critical in understanding the history of Gondwana amalgamation (e.g., Collins and Windley, 2002; Sajeev and Osanai, 2004; Santosh et al., 2009a,b, 2012, 2013, 2014, 2016, 2017; Dunkley et al., 2014; Tsunogae et al., 2014, 2015, 2016; He et al., 2015, 2016a,b; Kazami et al., 2016; Takamura et al., 2016, 2018; Endo et al., 2017;

* Corresponding author. Graduate School of Life and Environmental Sciences, University of Tsukuba, Ibaraki 305-8572, Japan.
E-mail address: tsunogae@geol.tsukuba.ac.jp (T. Tsunogae).
Peer-review under responsibility of China University of Geosciences (Beijing).

https://doi.org/10.1016/j.gsf.2018.05.019

Takahashi et al., 2018). These regions are regarded as parts of the Kuunga Orogen, which corresponds to an E–W trending orogenic belt formed by the assembly of Archean to Early Neoproterozoic continental fragments including Kalahari, Congo, Azania, East Antarctica, and Australia during 570–530 Ma (Meert et al., 1995; Meert and Lieberman, 2008) (Fig. 1). However, recent geochronological studies proposed slightly older metamorphic ages from the Highland Complex in Sri Lanka (~640 Ma; Takamura et al., 2015), the Palghat-Cauvery Suture Zone in southern India (~650 Ma; Koizumi et al., 2014), and the Lützow-Holm Complex in East Antarctica (650–580 Ma; Kawakami et al., 2016) in the Kuunga Orogen, suggesting that further geochronological investigations for the orogen are necessary to unravel multiple collisional events during Gondwana assembly.

The Zambezi Belt, exposed in northeastern Zimbabwe and southern Zambia as a western extension of the Kuunga Orogen (Fig. 1; Meert et al., 1995), is known for exposures of regionally metamorphosed meta-igneous and meta-supracrustal rocks possibly formed by collision of the Kalahari and Congo Cratons (e.g., Unrug, 1983; Coward and Daly, 1984; Porada and Berhorst, 2000; John et al., 2004). It is located in the southern margin of the Kalahari-Congo suture, immediately north of the Archean granite-greenstone terrane of the Zimbabwe Craton (Fig. 2a). The available structural data suggest that the boundary between the Zambezi Belt and the Zimbabwe Craton is defined by a shear zone along which the Zambezi Belt thrusted onto the Zimbabwe Craton (Dirks and Jelsma, 2006). The dominant lithologies of the belt are orthogneiss (biotite ± hornblende gneiss) and various metasedimentary and metavolcanic rocks. Available geochemical and geochronological data for orthogneisses indicate that their protoliths were formed by Tonian (870–850 Ma; e.g., Mariga et al., 1998; Mariga, 1999; Vinyu et al., 1999) and Stenian (1050 Ma; e.g., Hargrove et al., 2003) within-plate magmatism (e.g., Barton et al., 1991; Munyanyiwa et al., 1997; Hargrove et al., 2003). Johnson et al. (2007) also reported ca. 2890, 2680, 1090, 880 Ma magmatic zircons from felsic orthogneisses in the Zambezi Belt in Zambia, and inferred that ca. 880 Ma magmatism is associated with intra-continental rift. Previous studies on metamorphism of the region reported the peak metamorphic conditions of 650–700 °C and 7–8 kbar from the eastern part and 610–670 °C and 9.3–10.4 kbar from the northwestern part of the belt (e.g., Dirks et al., 1998; Hargrove et al., 2003), suggesting amphibolite-facies peak metamorphism at middle to lower crustal level and pressure increase from east to west. John et al. (2003) reported eclogite-facies rocks (2.6–2.8 GPa and 630–690 °C) from the western part of the Zambezi Belt in Zambia. The timing of peak metamorphism has been dated at 560–520 Ma (e.g., Margia, 1999; Vinyu et al., 1999; Goscombe et al., 2000; John et al., 2004). However, the available petrological and geochronological data of the Zambezi Belt are still limited and are not sufficient to unravel the tectonothermal evolution of the belt, and allow regional correlation of orogenic events in the Kuunga Orogen.

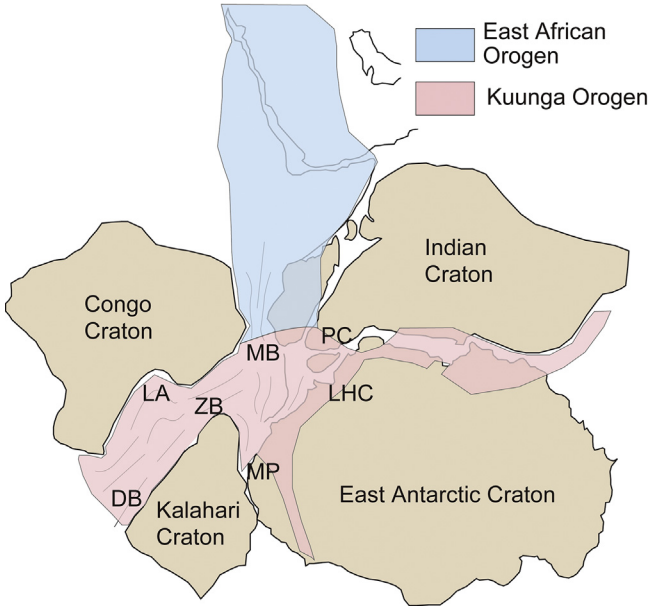

Figure 1. Simplified map showing the location of East Africa Orogen and Kuunga Orogen with representative cratons and orogens in East Gondwana (after Meert, 2003). DB: Damara Belt, LA: Lufilian Belt, LHC: Lützow-Holm Complex, MB: Mozambique Belt, MP: Maud Province, PC: Palghat-Cauvery Suture Zone, ZB: Zambezi Belt.

In this study, we report new petrological, geochemical, and U–Pb geochronological data of magmatic and detrital zircons for selected samples from the Zambezi Belt exposed in northeastern Zimbabwe, and confirmed Neoarchean (2655 ± 21 Ma) crustal growth related to within-plate magmatism possibly under continental rift setting, and subsequent latest Neoproterozoic (557–555 Ma) high-grade metamorphism possibly related to the collisional event of the Kalahari and Congo Cratons. Tonian (813 ± 5 Ma) within-plate magmatism reported in previous studies was also confirmed in this study. This study also presents the first detrital zircon ages from the Zambezi Belt, compares their age spectra with available geochronological data from adjacent orogens (e.g., Mozambique Belt, Damara Belt), and evaluates their implications on paleogeographic correlations. Such information is vital for evaluating the tectonics of terrane assembly and continent-continent collision during the Late Neoproterozoic–Cambrian orogeny in southern Africa, associated with the final assembly of the Gondwana supercontinent.

2. Geological setting

2.1. Regional geology and metamorphism

The Zambezi Belt, located between the Congo and Kalahari Cratons in southern Africa, is dominantly composed of felsic orthogneiss (biotite gneiss/schist, charnockite, enderbite, migmatite, meta-rhyolite, meta-quartz diorite, and meta-monzonite), metasediments (mica schist, psammitic gneiss, quartzite, kyanite-sillimanite schist, and marble), and metabasites (metagabbro, metapyroxenite, mafic granulite, and amphibolite) (e.g., Leitner and Phaup, 1974; Bache et al., 1982; Barton et al., 1991). Previous structural studies divided the Zambezi Belt into three domains; the Migmatitic Gneiss Terrain, Marginal Gneiss Terrain, and Allochthonous Gneiss Terrain from south to north (Fig. 2b; Barton et al., 1991; Dirks et al., 1998). The Migmatitic Gneiss Terrain is composed of high-grade metamorphic rocks (e.g., charnockite, biotite gneiss, pelitic gneiss, and amphibolite) overprinted during Pan African orogenic events (Barton et al., 1991). The Marginal Gneiss Terrain consists of Proterozoic metasediments (e.g., biotite gneiss, mica schist, metaquartzite, and marble), tectonically interleaved with orthogneiss units (e.g., amphibolite, metabasite, and mafic granulite) (Barton et al., 1991, 1993; Carney et al., 1991). The Allochthonous Terrain consists of felsic and mafic gneiss units (e.g., amphibolite, metagabbro, metapyroxenite, and biotite gneiss) that underwent intense deformation and metamorphism (Barton et al., 1991; Müller, 2004). The Allochthonous Terrain structurally overlies the Marginal Gneiss Terrain together with reworked basement gneiss, whereas the Marginal Gneiss Terrain tectonically overlies the Migmatitic Gneiss Terrain (Dirks and Jelsma, 2006). The Marginal and Migmatitic Gneiss Terrains are intruded by a sheet-like granitoid batholith (Basal Ruchinga Intrusive Complex).

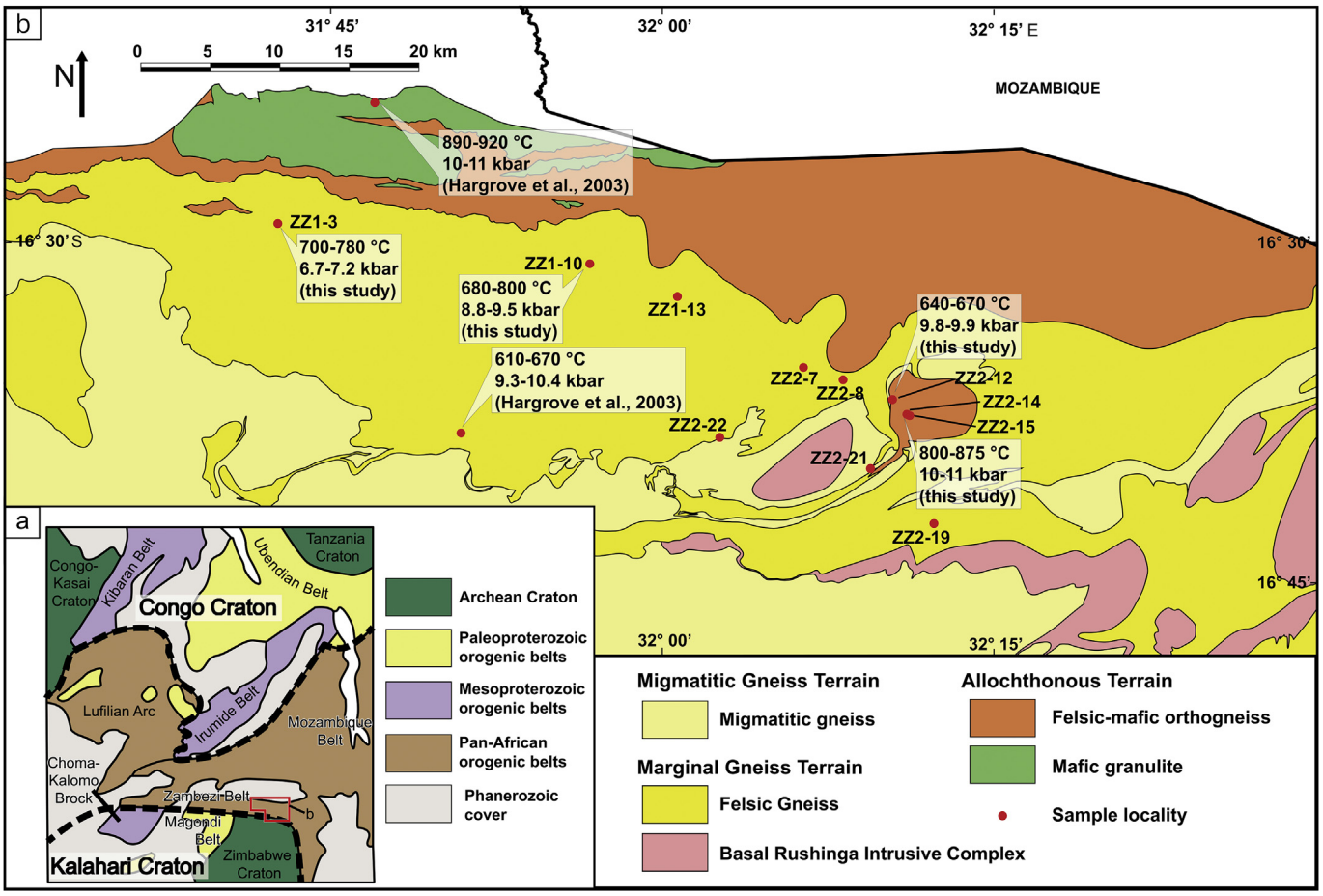

Figure 2. (a) Simplified tectonic subdivision of cratons and orogens around the Zambezi Belt, southern Africa (after Hanson, 2003). (b) Simplified geological map of the Zambezi Belt in northeastern Zimbabwe (after Leitner and Phaup, 1974; Bache et al., 1982; Barton et al., 1991), with locality of samples and calculated *P-T* conditions.

Available geochemical data for felsic orthogneisses from the western part of the Zambezi Belt indicates A-type and within-plate granitic affinities for the protolith, suggesting magmatism in a continental rift setting (Barton et al., 1991; Carney et al., 1991; Munyanyiwa et al., 1997; Hargrove et al., 2003; Katongo et al., 2004). Geochemical data of mafic orthogneisses plotted on discrimination diagrams show various signatures such as within-plate, MORB, or volcanic arc settings, and REE data suggest within-plate setting (Munyanyiwa et al., 1997).

Previous petrological and pressure-temperature (*P-T*) data of the Zambezi Belt indicate amphibolite-facies peak metamorphism (e.g., Treloar and Kramers, 1989; Carney et al., 1991). Dirks et al. (1998) reported peak *P-T* conditions of 650–670 °C and 6–7 kbar from the Marginal Gneiss Terrain in Zimbabwe, whereas Hargrove et al. (2003) reported higher-pressure conditions of 610–670 °C and 9.3–10.4 kbar for the same terrain. Similar high-pressure peak conditions of 685–725 °C and 9–11 kbar, and a clockwise *P-T* path were obtained for the Allochthonous Terrain in Zambia (John et al., 2004). John et al. (2003) reported eclogite-facies rocks (2.6–2.8 GPa and 630–690 °C) from the western part of the Zambezi Belt in Zambia. All the *P-T* data suggest pressure increase from east to west within the belt.

2.2. Geochronology

Previous geochronological studies of the Zambezi Belt suggest late Neoproterozoic to early Cambrian high-grade metamorphism (e.g., Barton et al., 1991, 1993; Mariga et al., 1998; Vinyu et al., 1999; Hargrove et al., 2003; John et al., 2004; Katongo et al., 2004; Johnson et al., 2007). Barton et al. (1991) reported Rb-Sr whole-rock errorchron dates of 699 ± 44 Ma and 468 ± 35 Ma from the Marginal Gneiss Terrain as the timing of uplifting and cooling of Pan-African orogeny (Barton et al., 1991, 1993). Vinyu et al. (1999) obtained the Ar-Ar ages of 525–491 Ma for hornblende in amphibolite from the Migmatitic Gneiss Terrain interpreted to record cooling. Hargrove et al. (2003) reported U-Pb zircon ages of ca. 550–530 Ma for metagabbro from the Allochthonous Gneiss Terrain interpreted to record timing of high-grade metamorphism. Goscombe et al. (2000) obtained a SHRIMP zircon age of 526 ± 17 Ma for orthogneisses from the Chewore Inliers in the Zimbabwean part of the Zambezi Belt and inferred Cambrian high-grade metamorphism. John et al. (2004) obtained 560–549 Ma monazite U-Pb ages for whiteschist from the Zambezi Belt in Zambia, and inferred latest Neoproterozoic peak metamorphism.

Several investigations on the emplacement ages of magmatic protoliths have also been carried out. Barton et al. (1991) reported Rb-Sr whole-rock errorchron ages of 823 ± 54 Ma and 823 ± 57 Ma from the Allochthonous Gneiss Terrain in Zimbabwe. Vinyu et al. (1999) studied biotite-hornblende gneiss in the Allochthonous Gneiss Terrain in Zimbabwe, and reported zircon and titanite U-Pb ages of ca. 870–850 Ma interpreted as a protolith age. Hargrove et al. (2003) reported U-Pb zircon ages for metagabbro from the Allochthonous Gneiss Terrain in Zimbabwe yielding igneous crystallization at ca. 1830 Ma. They also obtained U-Pb zircon ages of ca. 1050–870 Ma for orthogneisses from different part of the Allochthonous Gneiss Terrain taken to record magmatic

crystallization ages. In contrast, zircon in orthogneiss from the Marginal Gneiss Terrain in Zimbabwe shows a younger U-Pb zircon IDTIMS age of 795 Ma interpreted to record timing of protolith crystallization (Hargrove et al., 2003). Johnson et al. (2007) reported ca. 2890, 2680, and 1090 Ma magmatic zircons from felsic orthogneiss from the Zambezi Belt in Zambia, and argued that the older zircons (ca. 2890 Ma and 2680 Ma) could have been derived from Archean basement rocks. They also reported U-Pb ages of ca. 880 Ma for an orthogneiss from the region, and suggested Tonian magmatism possibly associated with Neoproterozoic crustal thinning and extension events.

3. Analytical method

3.1. Petrography and mineral chemistry

Polished thin sections were prepared for petrographic study at the University of Tsukuba, Japan. Mineral chemical analyses were carried out using an electron microprobe analyzer (JEOL JXA8530F) at the Chemical Analysis Division of the Research Facility Center for Science and Technology, the University of Tsukuba. The analyses were performed under conditions of 15 kV accelerating voltage and 10 nA sample current for all minerals, and the data were regressed using an oxide-ZAF correction program supplied by JEOL.

3.2. Whole-rock geochemistry

Representative fresh samples of felsic to mafic orthogneiss were selected for whole-rock geochemical analyses. We selected rocks with no obvious texture of partial melting and melt extraction, particularly in the case of felsic orthogneisses, to avoid the effect of element mobility and modification of primary geochemical signatures during high-grade metamorphism. The size of the samples was initially reduced in a jaw crusher, and then manually fine-powdered in an agate mortar. Major oxides were analyzed by 'lithium metaborate/tetraborate fusion ICP whole rock (Code 4B)', and minor and trace element by 'trace element ICP/MS (Code 4B2)' techniques at Activation Laboratories of Ontario, Canada. Fused samples were diluted and analyzed by Perkin Elmer Sciex ELAN 6000, 6100 or 9000 ICP/MS. Three blanks and five controls (three before sample group and two after) were analyzed per group of samples. Duplicates were fused and analyzed every 15 samples. The instrument was calibrated every 40 samples. Detection limits of major elements were 0.01%, where those of REE were 0.002–0.05 ppm. Detailed analytical conditions and detection limits are summarized in http://www.actlabs.com/.

3.3. Zircon U-Pb geochronology

Zircon U-Pb dating was performed by laser ablation-inductive coupled plasma-mass spectrometry (LA-ICP-MS). Detailed procedures for zircon separation and U-Pb analyses are summarized in Tsutsumi et al. (2012). Zircon grains were separated by heavy liquid (diiodo-methane) and magnetic separation from crushed rock samples, and then purified by hand picking under a binocular microscope. Zircon grains from the studied samples and standard materials were mounted in epoxy resin disc and polished until the surface was flattened with the center of the grains exposed. The FC1 zircon ($^{206}Pb/^{238}U = 0.1859$; Paces and Miller, 1993) and NIST SRM 610 standard glass were used as standard materials. Backscattered electron and cathodoluminescence (CL) images were obtained using scanning electron microprobe–cathodoluminescence (SEM-CL) equipment, JSM-6610 (JEOL) and a CL detector (SANYU electron), installed at the National Museum of Nature and Science, Japan. U-Th-Pb isotopic analyses were carried out using LA-ICP-MS (Agilent 7700x with ESI NWR213 laser ablation system) installed at the National Museum of Nature and Science, Japan. A Nd-YAG laser with a 213 nm wavelength and 5 ns pulse was used for the analysis. A 25-μm spot size and 4–5 J/cm^2 laser power were adopted in this study. He gas was used as the carrier gas instead of Ar gas to enhance a higher transport efficiency of ablated materials (e.g., Eggins et al., 1998). Common Pb corrections for the concordia diagrams and for each age were made using ^{208}Pb (Williams, 1998), on the basis of the model for common Pb compositions proposed by Stacey and Kramers (1975). The upper and lower intercepts in the concordia diagram were calculated using the Isoplot4.15/Ex software (Ludwig, 2008).

4. Results

4.1. Petrography

A brief summary of petrographic features of representative samples examined for petrological, geochemical, and zircon geochronological studies, is described below. Representative field photographs and photomicrographs of the rocks are shown in Figs. 3 and 4, respectively. Mica schist (pelitic schist) is characterized by obvious foliation in hand specimen defined by aligned micaceous minerals (Fig. 3a). Medium-grained amphibolite (Fig. 3b), which is a dominant mafic orthogneiss in the study area, occurs as layers in felsic orthogneiss. Felsic orthogneiss is characterized by strong foliation defined by alternation of biotite-rich and quartzo-feldspathic layers (Fig. 3c and d), and rarely contains boudins of meta-ultramafic rock (Fig. 3c). The approximate mineral assemblages of the studied pelitic schist, mafic orthogneiss, meta-ultramafic rock, and felsic orthgneiss and paragneiss samples are summarized in Table 1.

4.1.1. Pelitic schist

Sample ZZ2-7A from the Marginal Gneiss Terrain is a typical example of muscovite schist. It is composed of quartz (80%–85%), muscovite (5%–10%), microcline (3%–5%), plagioclase (3%–5%), and biotite (1%), with accessory zircon and apatite (Fig. 4a). Quartz is coarse grained (0.3–3 mm), poikiloblastic, and often contains inclusions of plagioclase, microcline, muscovite, biotite, apatite, and zircon. Plagioclase and microcline are medium grained (0.1–1 mm) and xenoblastic to subidioblastic, and occur in the matrix or as inclusions in quartz. Muscovite occurs as medium grained (0.1–1.2 mm) lepidoblastic flakes, and often intergrows with fine-grained (0.1–0.3 mm, up to 1.5 mm) and subidioblastic biotite, forming the foliation of the rock. Zircon is fine grained (0.1–0.3 mm) and rounded, and mostly present within quartz.

4.1.2. Mafic orthogneiss

Two mafic orthogneiss (amphibolite) samples (one from the Allochthonous Terrain and another from the Marginal Gneiss Terrain) were examined in this study. Sample ZZ2-14A from the Allochthonous Terrain is a fine-grained amphibolite with calcic amphibole (50%–55%), plagioclase (40%–50%), biotite (1%–3%), garnet (<1%), quartz (<1%), and accessory Fe-Ti oxide (mainly magnetite) (Fig. 4b). Foliation is not obvious. Dark greenish to brownish calcic amphibole occurs as fine-grained (0.1–0.5 mm) and subidioblastic to xenoblastic mineral in the matrix, although coarse-grained porphyroblastic amphibole of ~2 mm in length is also present. Plagioclase is fine grained (0.1–0.3 mm), xenoblastic, and occurs in the matrix. Biotite is fine grained (0.05–0.3 mm), and rarely present as intergrowth with calcic amphibole or as inclusions in plagioclase. Garnet is also fine grained (0.05–0.1 mm), subidioblastic to rounded, and always

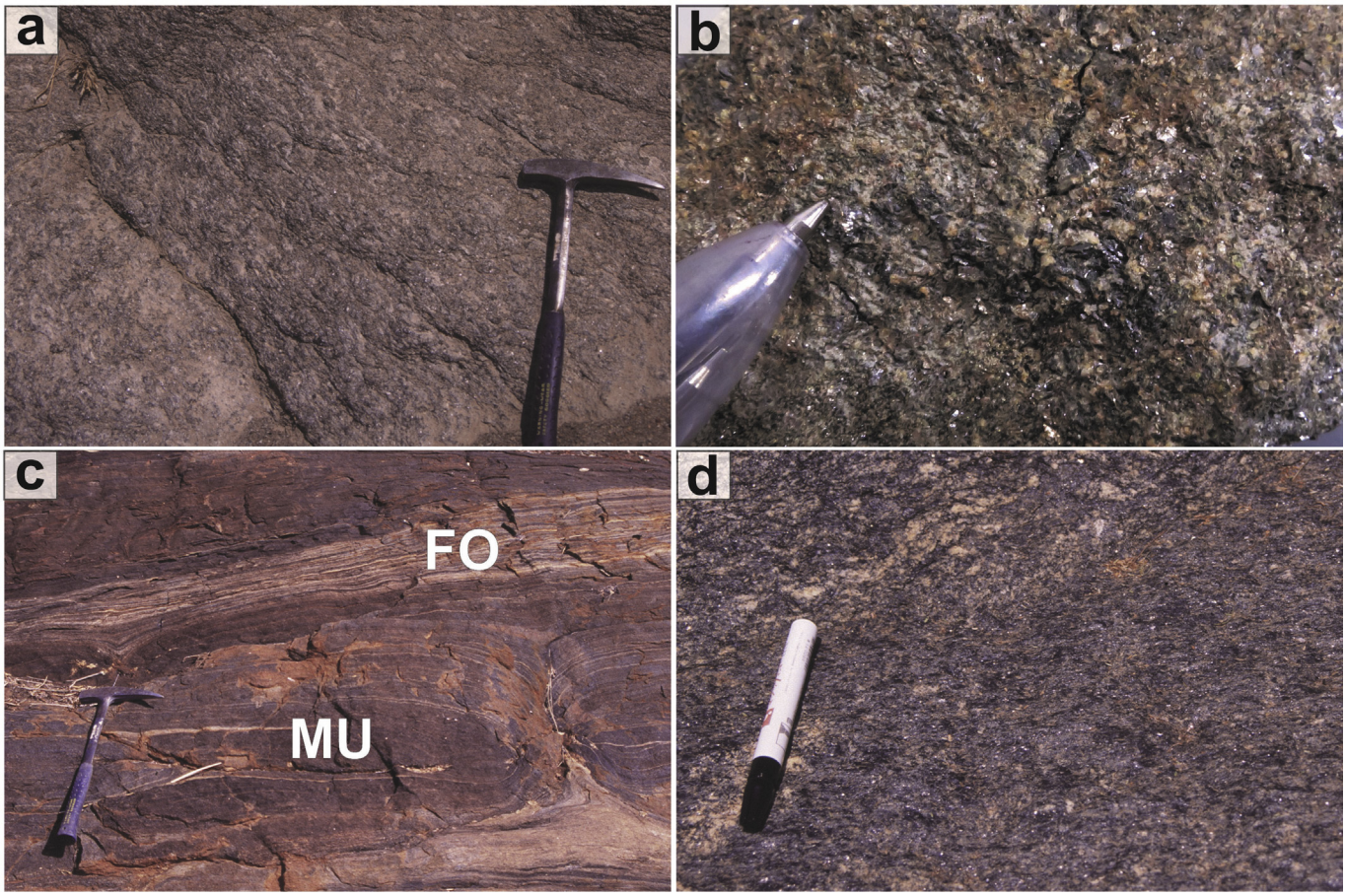

Figure 3. Field photographs of representative lithologies discussed in this study. (a) Pelitic schist with obvious foliation defined by aligned micaceous minerals. (b) Amphibolite (mafic orthogneiss). (c) Boudins of meta-ultramafic rock (MU) in felsic orthogneiss (FO). (d) Biotite gneiss (felsic orthogneiss) with obvious gneissosity defined by alternation of biotite-rich and quartzo-feldspathic layers.

associated with calcic amphibole and plagioclase. Quartz is fine grained (0.3–0.6 mm), xenoblastic, and fills the matrix of calcic amphibole and plagioclase.

Sample ZZ2-19A from the south-easternmost part of the study area is a biotite-rich and coarse-grained amphibolite of the Marginal Gneiss Terrain. It is composed of plagioclase (35%–40%), calcic amphibole (25%–30%), biotite (25%–30%), titanite (1%–3%), quartz (<1%), and accessory apatite (Fig. 4c). Foliation of the rock is defined by aligned calcic amphibole and biotite as well as elongated plagioclase grains. Plagioclase is fine to coarse grained (0.1–1.5 mm), subidioblastic to xenoblastic or elongated, and present as a matrix phase, although rare plagioclase inclusions occur in titanite. Calcic amphibole is medium to coarse grained (0.2–2 mm), subidioblastic, dark greenish to light greenish in color as the dominant ferromagnesian mineral in the rock, although fine-grained amphibole also occurs as inclusions in quartz. Biotite is medium to coarse grained (0.2–2 mm), subidioblastic, and often intergrows with calcic amphibole and fine-grained (0.1–0.3 mm) and subidioblastic titanite. Quartz is rare, and occurs along grain boundaries of plagioclase and calcic amphibole.

4.1.3. Meta-ultramafic rock

Sample ZZ2-12 is a garnet-rich hornblendite of the Allochthonous Terrain, collected close to the boundary with the Marginal Gneiss Terrain. It is composed of garnet (50%–55%), calcic amphibole (40%–45%), and Fe-Ti oxide (magnetite and ilmenite; 10%–15%) (Fig. 4d). Garnet and calcic amphibole are granoblastic matrix minerals showing semi-equigranular texture. They also occur as inclusions in each other, suggesting both garnet and hornblende were formed together during high-grade (possibly peak) metamorphism. Garnet is fine to medium grained (0.1–1 mm), subidioblastic to rounded, and pale pinkish in color. Calcic amphibole is also fine to medium grained (0.1–1 mm), xenoblastic to subidioblastic, and dark greenish to light greenish in color. Fe-Ti oxide fills the matrix of the garnet and amphibole possibly as a later product.

Sample ZZ2-15A is an another variety of meta-ultramafic rock, marked as 'metapyroxenite' of the Allochthonous Terrain in the geological map of the study area (Barton et al., 1991). It is composed of calcic amphibole (35%–40%), plagioclase (30%–35%), orthopyroxene (5%–10%), cummingtonite (5%–10%), spinel (1%–5%), magnetite (5%–10%), and garnet (<1%) (Fig. 4e). Calcic amphibole is fine to medium grained (0.1–1 mm), subidioblastic, greenish to pale greenish in color, and often associated with spinel and magnetite. Plagioclase in the matrix is medium grained (0.1–0.5 mm) and xenoblastic. Orthopyroxene is present as coarse-grained (2–2.5 mm) and subidioblastic porphyroblast-like minerals probably as a relict magmatic phase. Cummingtonite is medium grained (0.5–1 mm), subidioblastic, and often intergrows with calcic amphibole. Dark greenish spinel is medium grained (0.3–0.8 mm), subidioblastic, and often showing composite grains with magnetite, suggesting post-peak exsolution of spinel from magnetite (e.g., Ishii et al., 2006; Shimizu et al., 2009).

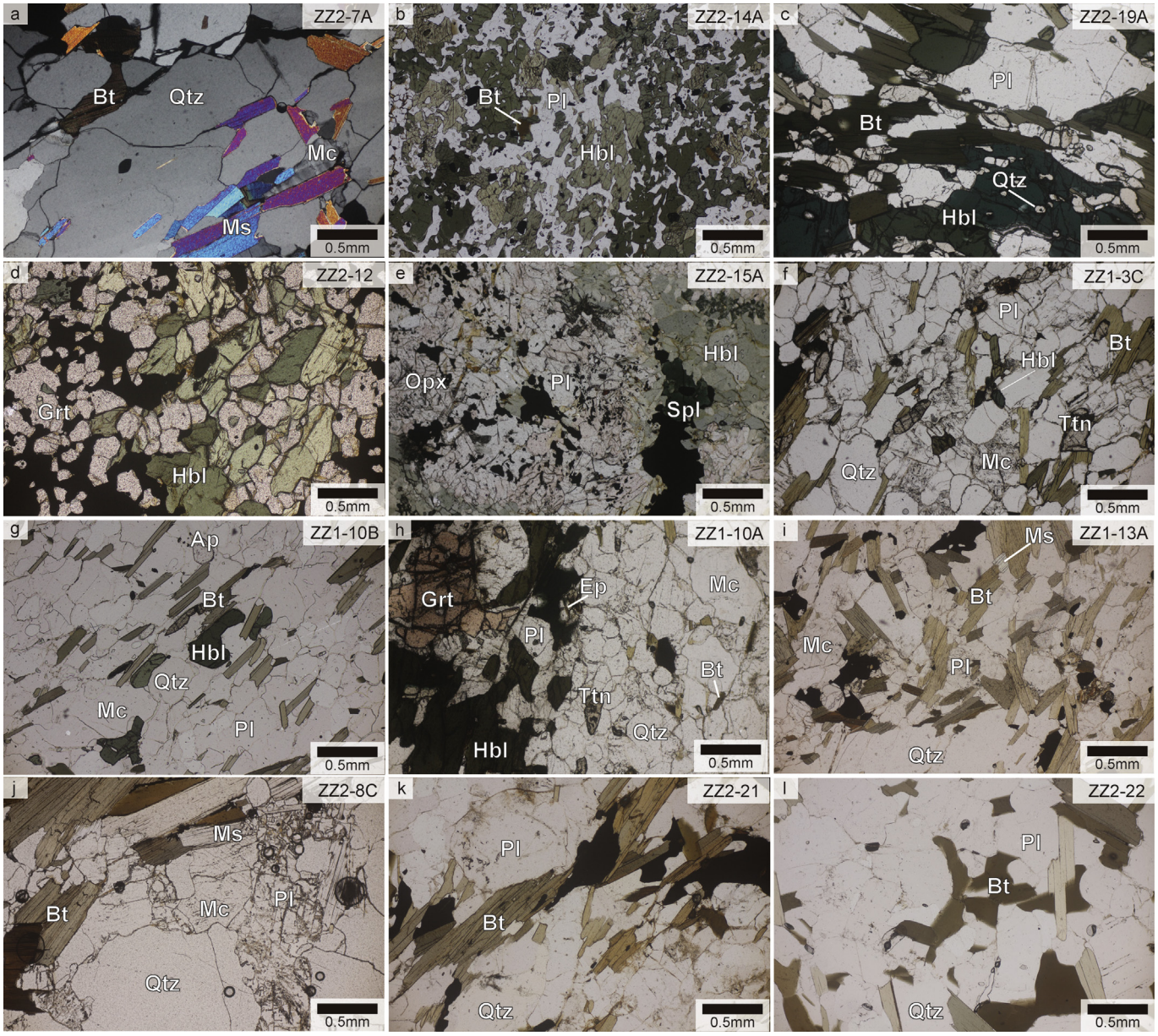

Figure 4. Representative photomicrographs showing mineral assemblages and textures of samples from the Zambezi Belt. See text for descriptions. (a) ZZ2-7A (pelitic schist), (b) ZZ2-14A (mafic orthogneiss), (c) ZZ2-19A (mafic orthogneiss), (d) ZZ2-12 (meta-ultramafic rock), (e) ZZ2-15A (metapyroxenite), (f) ZZ1-3C (felsic orthogneiss), (g) ZZ1-10B (felsic orthogneiss), (h) ZZ1-10A (felsic orthogneiss), (i) ZZ1-13A (felsic orthogneiss), (j) ZZ2-8C (felsic orthogneiss), (k) ZZ2-21 (felsic paragneiss), (l) ZZ2-22 (felsic paragneiss). Ap: apatite, Bt: biotite, Ep: epidote, Grt: garnet, Hbl: hornblende, Mc: microcline, Ms: muscovite, Opx: orthopyroxene, Pl: plagioclase, Qtz: quartz, Spl: spinel, Ttn: titanite.

4.1.4. Felsic orthogneiss

Five felsic orthogneiss samples were examined in this study. Sample ZZ1-3C from the Marginal Gneiss Terrain in the western part of the study area is a fine-grained meta-granodioritic rock with plagioclase (25%–30%), microcline (20%–25%), quartz (25%–30%), biotite (10%–15%), titanite (2%–3%), calcic amphibole (1%), and accessory zircon and magnetite (Fig. 4f). Foliation of the rock is defined by thin alternation of biotite-rich and quartz-feldspathic layers. Quartz, plagioclase, and microcline are all fine to medium grained (0.1–1 mm) and show granoblastic texture. Biotite occurs as fine-grained (0.2–0.5 mm) and subidioblastic flakes along the grain boundaries of the quartzo-feldspathic minerals, although it is also present as inclusions in plagioclase. Titanite is idioblastic to subidioblastic, fine grained (0.2–0.5 mm), and often intergrows with biotite. Greenish-brown calcic amphibole is subidioblastic, medium grained (0.4–1 mm), and also intergrows with the biotite. Zircon is fine grained (<0.1 mm) and rounded.

Sample ZZ1-10B (Fig. 4g) collected from a different locality in the central part of the study area but in the same rock unit also shows similar petrological characters as sample ZZ1-3C. In contrast, sample ZZ1-10A from the same locality is a garnet-bearing variety, and is composed of quartz (35%–40%), microcline (25%–30%), plagioclase (5%–10%), calcic amphibole (5%–10%), biotite (5%–10%), garnet (1%–3%), and epidote (<1%), with accessory titanite, zircon, and ilmenite (Fig. 4h). Quartz and microcline in the matrix are xenoblastic and fine grained (0.1–0.7 mm). Plagioclase also occurs as xenoblastic and fine grained (0.3–0.8 mm) matrix mineral. Biotite is medium grained (0.1–0.8 mm), subidioblastic, and weakly elongated along the rock foliation. Xenoblastic to subidioblastic and fine to medium grained (0.2–1 mm) calcic amphibole and epidote

Table 1
Location, rock type and mineralogy of samples from the Zambezi Belt used for geochemistry, geothermobarometry, and U-Pb geochronology.

Sample No.	Geological unit	Co-ordinates	Lithology	Mineral assemblage
ZZ1-3C	Marginal Gneiss Terrain	S16°29′20″; E31°42′27″	Felsic orthogneiss	Pl Mc Qtz Bt Ttn Hbl Zrn Mag
ZZ1-10A	Marginal Gneiss Terrain	S16°31′6″; E31°56′39″	Felsic orthogneiss	Qtz Mc Pl Hbl Bt Grt Ep Ttn Zrn Ilm
ZZ1-10B	Marginal Gneiss Terrain	S16°31′6″; E31°56′39″	Felsic orthogneiss	Pl Mc Qtz Bt Ttn Hbl Zrn Ilm
ZZ1-13A	Marginal Gneiss Terrain	S16°32′29″; E32°0′47″	Felsic orthogneiss	Qtz Pl Mc Bt Ms Ap Zrn Ilm
ZZ2-7A	Marginal Gneiss Terrain	S16°35′33″; E32°6′34″	Pelitic schist	Qtz Ms Mc Pl Bt Ap Zrn
ZZ2-8C	Marginal Gneiss Terrain	S16°36′4″; E32°8′18″	Felsic orthogneiss	Qtz Pl Mc Bt Ms Ap Zrn Ilm
ZZ2-12	Allochthonous Terrain	S16°37′1″; E32°10′37″	Meta-ultramafic rock	Grt Hbl Mag Ilm
ZZ2-14A	Allochthonous Terrain	S16°37′40″; E32°11′16″	Mafic orthogneiss	Hbl Pl Bt Grt Qtz Mag
ZZ2-15A	Allochthonous Terrain	S16°37′44″; E32°11′24″	Meta-ultramafic rock	Hbl Pl Opx Cum Spl Mag Grt
ZZ2-19A	Marginal Gneiss Terrain	S16°42′25″; E32°12′30″	Mafic orthogneiss	Pl Hbl Bt Ttn Qtz Ap
ZZ2-21	Marginal Gneiss Terrain	S16°40′2″; E32°9′37″	Felsic paragneiss	Qtz Pl Bt Zrn Rt Ap Mag
ZZ2-22	Marginal Gneiss Terrain	S16°38′42″; E32°2′41″	Felsic paragneiss	Qtz Pl Bt Zrn Rt Ap Mag

(0.1–0.3 mm) intergrow with the biotite, although coarse-grained calcic amphibole of 1.2–2.0 mm in length is also present in the matrix. Garnet is medium to coarse grained (0.8–2 mm), subidioblastic, and rarely contains fine-grained (0.05–0.2 mm) inclusions of quartz.

Sample ZZ1-13A from the Marginal Gneiss Terrain is lithologically different from sample ZZ1-10A, and is marked as 'layered migmatitic gneiss' in the geological map of the study area (Leitner and Phaup, 1974). The rock is a fine- to medium-grained metagranitic rock with quartz (50%–55%), plagioclase (15%–20%), microcline (15%–20%), biotite (10%–15%), muscovite (1%), and accessory apatite, zircon, and ilmenite (Fig. 4i). Quartz and plagioclase are fine to medium grained (0.1–1 mm) and xenoblastic, although coarse-grained quartz of ~2 mm in length is also present. Microcline is fine grained (0.1–0.5 mm) and xenoblastic, and is present as a matrix mineral. Muscovite is fine grained (0.1–0.2 mm), subidioblastic, and often intergrows with fine-grained (0.2–0.5 mm) subidioblastic flakes of biotite. Apatite is fine grained (0.1–0.2 mm) and subidioblastic. Zircon is fine grained (0.1–0.3 mm) and rounded, and is mostly present within quartz and biotite. Sample ZZ2-8C, which also belongs to the Marginal Gneiss Terrain, shows similar petrological character, except its coarser grained size (Fig. 4j) than sample ZZ1-13A.

4.1.5. Felsic paragneiss

Two felsic paragneiss samples were examined in this study. Sample ZZ2-21 (Fig. 4k) from the Marginal Gneiss Terrain in the southeastern part of the study area was collected from a locality close to the boundary with the Allochthonous Terrain. It is composed of quartz (60%–65%), plagioclase (5%–10%), and biotite (25%–30%), with accessory zircon, rutile, apatite, and magnetite. Quartz and plagioclase are fine to coarse grained (0.2–2 mm) and xenoblastic. The coarse-grained quartz often contains inclusions of plagioclase, biotite, and zircon. Biotite is fine to coarse grained (0.1–3 mm), subidioblastic, and dominantly occurs together with magnetite. Zircon is fine grained (0.1–0.3 mm), rounded, and often occurs within quartz and biotite. Apatite is fine grained (0.1–0.2 mm) and subidioblastic. Sample ZZ2-22 from the same region also shows similar mineral assemblages and petrological characters (Fig. 4l).

4.2. Mineral chemistry

Representative mineral compositions obtained by electron microprobe analyses are given in Supplementary Tables 2–5, plotted in Fig. 5, and briefly described below. The samples selected for the microprobe analyses are used for geothermobarometry, whole-rock geochemistry, and zircon U-Pb geochronology.

4.2.1. Calcic amphibole

Calcic amphibole in meta-ultramafic samples is Mg-rich (X_{Mg} = Mg/(Fe + Mg) = 0.52–0.73), and is classified as pargasite (Si = 6.12–6.21 pfu, Ti = 0.07–0.10 pfu, Ca = 1.68–1.85 pfu; Fig. 5a, Supplementary Table 2) based on the classification of Leake et al. (1997). The pargasite in sample ZZ2-15A shows the highest X_{Mg} (0.71–0.73) and moderate $(Na + K)_A$ content of 0.79–0.85 pfu, whereas that in sample ZZ2-12 contains lower $(Na + K)_A$ of 0.53–0.54 pfu.

Calcic amphiboles in mafic orthogneisses are all classified as ferro-pargasite (X_{Mg} = 0.31–0.51, Si = 6.14–6.41 pfu, Ti = 0.04–0.21 pfu, Ca = 1.83–1.92 pfu, $(Na + K)_A$ = 0.87–0.99 pfu). The ferro-pargasite in sample ZZ2-14A (amphibolite) shows higher $(Na + K)_A$ (0.95–0.99 pfu), Ti (0.16–0.21 pfu) contents, and X_{Mg} (0.45–0.51), and slightly lower Si (6.14–6.33 pfu) and Ca (1.83–1.88 pfu) contents. In contrast, ferro-pargasite in sample ZZ2-19A (amphibolite) shows slightly higher Si (6.83–6.41 pfu) and Ca (1.88–1.92 pfu) contents, and lower $(Na + K)_A$ (0.87–0.91 pfu), Ti (0.04–0.05 pfu) contents, and X_{Mg} (0.31–0.33).

Calcic amphiboles in felsic orthogneiss are also classified as ferro-pargasite (X_{Mg} = 0.17–0.39, Si = 6.08–6.37 pfu, Ti = 0.06–0.12 pfu, Ca = 1.78–1.97 pfu, $(Na + K)_A$ = 0.76–1.03 pfu), but they are slightly lower in X_{Mg} than those in mafic orthogneisses and meta-ultramafic rocks. The ferro-pargasite in sample ZZ1-10B (meta-granodioritic rock) shows the highest Si content (6.28–6.37 pfu) and X_{Mg} (0.39), whereas that in sample ZZ1-10A (garnet-bearing meta-granodioritic rock) displays the lowest Si content (6.08–6.21 pfu) and X_{Mg} (0.17–0.22). The ferro-pargasite in sample ZZ1-3C (meta-granitic rock) shows high Si content (6.32–6.33 pfu) and moderate X_{Mg} (0.21).

4.2.2. Biotite

Biotite in pelitic schist (sample ZZ2-7A) shows the highest TiO_2 content of 3.3–3.5 wt.% and the lowest X_{Mg} of 0.14 (Fig. 5b; Supplementary Table 3). That in mafic rock (sample ZZ2-19A) shows the lowest TiO_2 content of 1.10–1.12 wt.%, and relatively higher X_{Mg} of 0.46–0.47. Biotite in felsic orthogneiss displays varying TiO_2 content and X_{Mg} of 1.28–2.88 wt.% and 0.26–0.51, respectively, whereas that in samples ZZ1-3C and ZZ1-10A (felsic orthogneiss) shows consistent X_{Mg} of 0.26–0.34. That in meta-granitic rock (samples ZZ1-10B and ZZ1-13A) is enriched in X_{Mg} as 0.45–0.51. Biotite in felsic paragneiss (samples ZZ2-21 and ZZ2-22) shows the highest X_{Mg} content of 0.54–0.59.

4.2.3. Pyroxenes

Orthopyroxene in meta-ultramafic rock (sample ZZ2-15A) is enriched in Mg (X_{Mg} = 0.78–0.79) and depleted in Ca and Al (CaO = 0.13–0.23 wt.%, Al_2O_3 = 1.30–3.36 wt.%) (Fig. 5c;

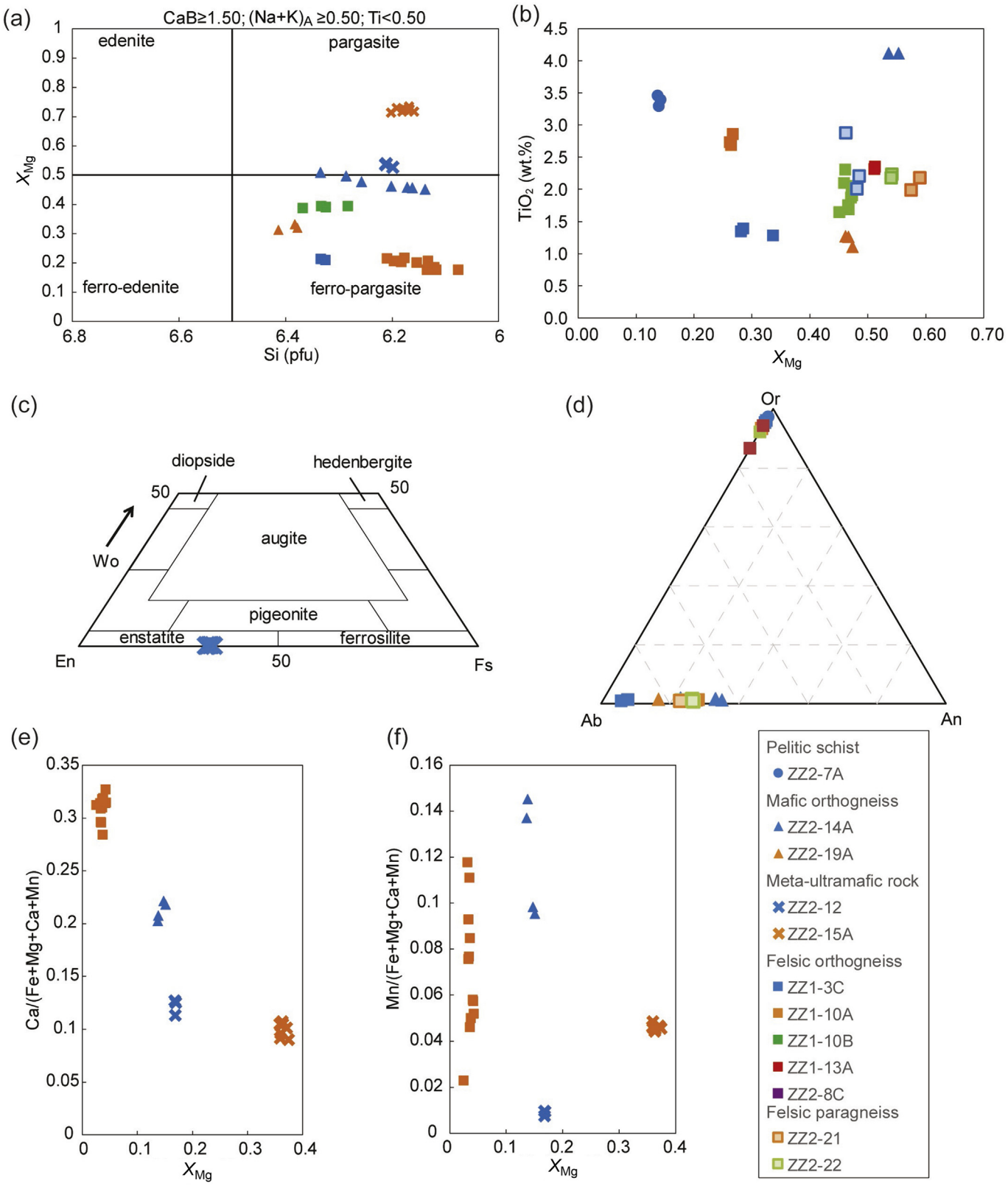

Figure 5. Compositional diagrams showing chemistry of representative minerals. (a) Si versus X_{Mg} diagrams showing composition of calcic amphibole. Classification of amphibole is after Leake et al. (1997). (b) X_{Mg} versus TiO_2 diagram showing biotite chemistry. (c) Triangular diagram showing pyroxene chemistry. (d) Triangular diagram showing feldspar chemistry. (e) Ca/(Fe + Mg + Ca + Mn) versus X_{Mg} diagram showing garnet chemistry. (f) Mn/(Fe + Mg + Ca + Mn) versus X_{Mg} diagram showing garnet chemistry.

Supplementary Table 2). No compositional zoning has been identified for the mineral.

4.2.4. Feldspars

Plagioclase in mafic orthogneiss (e.g., sample ZZ2-14A) shows a wide compositional range of $An_{22–32}$, probably reflecting different protolith compositions (Fig. 5d; Supplementary Table 4). On the other hand, plagioclase in felsic orthogneiss and paragneiss samples (ZZ1-10A, ZZ1-10B, and ZZ2-22) shows consistent albite-rich compositions of $An_{23–28}$, except one sample (ZZ1-3C) with extremely high albite content of $An_{6–7}$, possibly formed by local albitization. All microcline grains in felsic gneiss samples show consistent orthoclase-rich compositions of $Or_{89–97}$.

4.2.5. Garnet

Garnet in mafic orthogneiss (sample ZZ2-14A), meta-ultramafic rocks (samples ZZ2-12 and ZZ2-15A), and felsic orthogneiss (sample ZZ1-10A) is principally almandine rich with minor grossular, pyrope, and spessartine components as $Alm_{56–58}Pyr_{9–10}Grs_{20–22}Sps_{10–15}$, $Alm_{72–73}Pyr_{14}Grs_{11–13}Sps_{1}$, $Alm_{54–55}Pyr_{30–32}Grs_{9–11}Sps_{4–5}$, and $Alm_{55–65}Pyr_{2–3}Grs_{28–33}Sps_{2–12}$, respectively (Fig. 5e and f; Supplementary Table 5). Garnet grains in meta-ultramafic rocks are compositionally nearly homogeneous, whereas those in mafic (sample ZZ2−14A) and felsic orthogneiss (sample ZZ1−10A) show slightly almandine-rich and spessartine-poor rims ($Alm_{58}Pyr_{10}Grs_{22}Sps_{10}$ and $Alm_{55–61}Pyr_{2}Grs_{30–31}Sps_{8–12}$, respectively) than cores ($Alm_{56–57}Pyr_{9}Grs_{20–21}Sps_{14–15}$ and $Alm_{59–65}Pyr_{2}Grs_{28–33}Sps_{2–6}$, respectively).

4.2.6. Spinel

Spinel in meta-ultramafic rock (sample ZZ2-15A) is characterized by high Mg (X_{Mg} = 0.54–0.69) and Al (1.93–1.97 pfu), and low Cr_2O_3 (0.01–0.8 wt.%) and Fe_2O_3 ($Fe^{3+}/(Fe^{2+}+Fe^{3+})$ = 0.08–0.17) contents. Its ZnO content is also low (0.45–1.17 wt.%) (Supplementary Table 5).

4.2.7. Muscovite

Muscovite in all samples exhibits compositions of Si = 6.22–6.42 pfu, Al^{vi} = 3.14–3.53 pfu, and FeO^T + MgO = 3.64–6.52 wt.%. The muscovite in pelitic schist (sample ZZ2-7A) is characterized by lower Si (6.22–6.29 pfu) and FeO^T + MgO (3.64–3.65 wt.%), and higher Al^{vi} (3.52–3.53 pfu) contents, whereas that in felsic orthogneisses (samples ZZ1-13A and ZZ2-8C) shows higher Si (6.37–6.42 pfu) and FeO^T + MgO (6.30–6.52 wt.%), and lower Al^{vi} (3.14–3.18 pfu) contents (Supplementary Table 5). Na content in the mineral is generally low (0.06–0.13 pfu).

4.3. Whole-rock geochemistry

The whole-rock geochemical data, including major, minor, trace, and rare earth elements, of eleven representative samples (two mafic orthogneisses, two meta-ultramafic rocks, five felsic orthogneisses, and two felsic paragneisses) are given in Supplementary Table 6. The geochemical features of the rocks are summarized below based on several compositional diagrams (Figs. 6–10).

4.3.1. Major and trace elements

The relationship between total alkali and SiO_2 (TAS) content can be utilized to classify igneous protolith (Fig. 6a). According to the TAS plot, the mafic orthogneiss and meta-ultramafic rock samples are mostly alkalic, whereas felsic orthogneisses are all sub-alkalic. In contrast, the Nb/Y versus Zr/TiO_2 diagram of Winchester and Floyd (1977) (Fig. 6b) indicates alkalic signatures for most of orthogneiss samples. Felsic orthogneisses are classified as granitic to quartz dioritic in the TAS diagram (Fig. 6a) and comenditic to rhyolitic in the Nb/Y–Zr/TiO_2 diagram (Fig. 6b). Mafic orthogneisses are gabbroic in the TAS diagram and trachyandesitic in the Nb/Y–Zr/TiO_2 diagram.

In Harker diagram (Fig. 7 after Wilson, 1989), mafic orthogneisses show low SiO_2 content of 45.0–47.2 wt.%, whereas felsic orthogneiss are enriched in SiO_2 as 64.4–70.4 wt.%. Meta-ultramafic rocks show the lowest SiO_2 content of 30.5–36.1 wt.%. The orthogneisses show a positive correlation of K_2O and Na_2O, and negative correlation of TiO_2, $Fe_2O_3{}^T$, MnO, and MgO with increasing silica content, suggesting fractional crystallization.

In the primitive-mantle normalized trace element plots (Sun and McDonough, 1989), the felsic orthogneisses are characterized

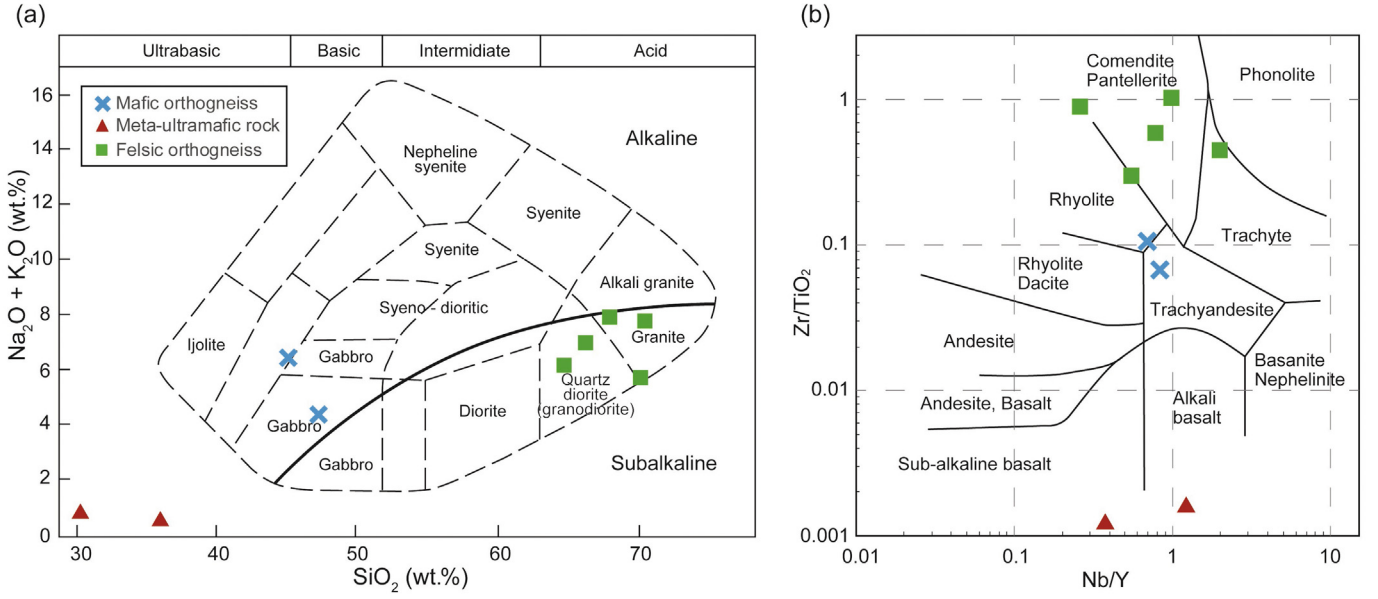

Figure 6. (a) Total alkali versus SiO_2 (TAS) diagram (after Wilson, 1989) showing the classification of orthogneisses from the Zambezi Belt. (b) Nb/Y versus Zr/TiO_2 diagram (after Winchester and Floyd, 1977) showing the classification of orthogneisses discussed in this study.

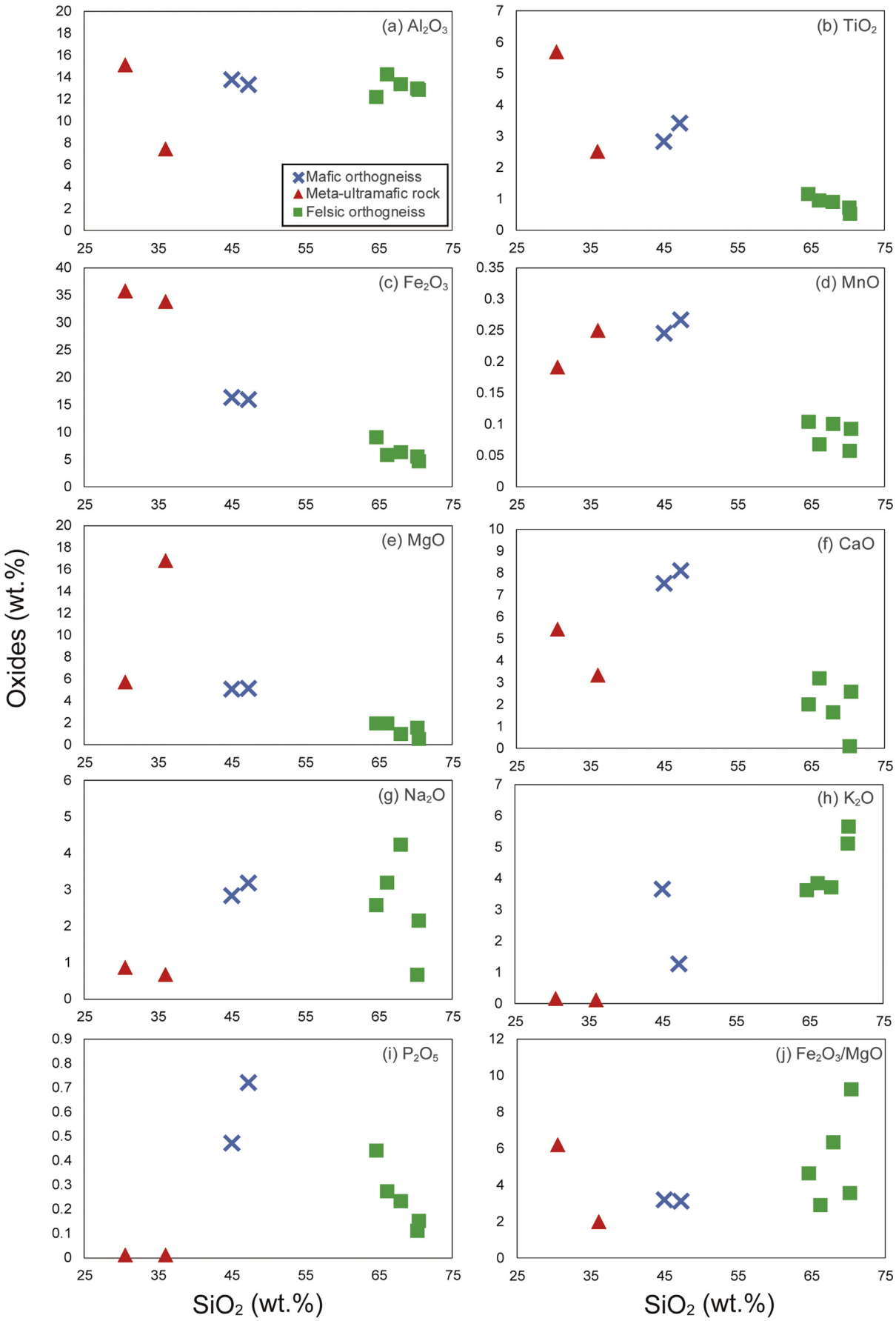

Figure 7. Major element variation diagrams (Harker diagram after Wilson, 1989) for felsic gneisses, mafic orthogneisses, and meta-ultramafic rocks from the Zambezi Belt.

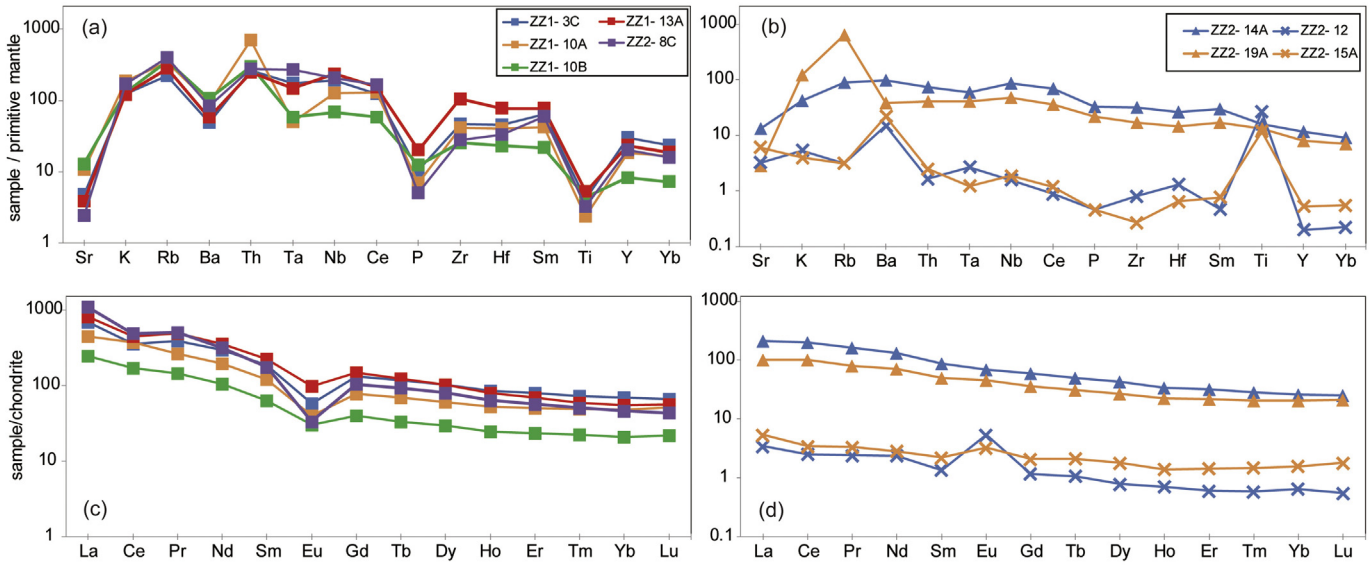

Figure 8. Primitive mantle-normalized multi-element variation diagrams for felsic (a) and mafic (b) orthogneisses. Normalizing values are from Sun and McDonough (1989). Chondrite-normalized REE spider plots for felsic (c), and mafic (d) orthogneisses. Normalizing values are from McDonough and Sun (1995).

by enrichment of large ion lithophile elements (LILEs) such as Rb, Ba and K, suggesting fractional crystallization. These rocks show negative Ta, P, and Ti anomalies and relatively constant high-field strength elements (HFSE; e.g., Zr, Hf) (Fig. 8a). Depletion of some HFSE might suggest that the rock formed in magmatic arcs or the magma interacted with continental crust (Foley et al., 2000). The mafic orthogneisses (Fig. 8b) are characterized by relatively flat patterns, similar to oceanic island basaltic signature, whereas an amphibolite (sample ZZ2-19A) shows enrichment of LILEs. The meta-ultramafic rocks are characterized by positive Ba and Ti anomalies.

In the chondrite normalized REE plot (Fig. 8c and d; McDonough and Sun, 1995), most felsic orthogneisses are characterized by enrichment of light REE (LREE) ($(La/Sm)_{cn}$ = 3.62–6.24) and flat heavy REE (HREE) patterns ($(Gd/Yb)_{cn}$ = 1.17–3.57), suggesting fractional crystallization. Some felsic orthogneisses show negative Eu anomaly, possibly suggesting plagioclase fractionation. Mafic orthogneisses and meta-ultramafic rocks are characterized by relatively enriched LREE ($(La/Sm)_{cn}$ = 2.04–2.52) and nearly flat HREE pattern ($(Gd/Yb)_{cn}$ = 1.32–2.30). Sample ZZ2-12 (meta-ultramafic rock) shows a positive Eu anomaly possibly related to plagioclase accumulation and/or crustal contamination.

4.3.2. Petrogenetic implications

The Nb-Y and Ta-Yb diagrams of Pearce et al. (1984) for granitic rocks (Fig. 9a and b) suggest that all the analyzed felsic orthogneiss samples fall either in the fields of within-plate granites (WPG) or in the overlapped field of WPG and ocean-ridge granites (ORG). According to the Rb–(Y + Nb) diagram of Pearce et al. (1984) for granitic rocks (Fig. 9c), all the felsic orthogneiss samples also fall in the field of WPG. The $(Nb/Zr)_N$–Zr diagram (Thiéblemont and Tegyey, 1994; Thiéblemont, 1999) for granitic rocks (Fig. 9d) suggests the signature of collision- or intraplate-related granitoid for all the felsic orthogneiss samples. The published geochemical data of felsic orthogneiss from the Zambezi Belt in Zimbabwe (Hargrove et al., 2003) are also plotted in the figure and show similar WPG affinity.

In the TiO_2–MnO–P_2O_5 triangular diagram (after Mullen, 1983), the mafic orthogneisses fall in the fields of MORB (sample ZZ2-14A), ocean-island alkali basalt, or seamount alkali basalt (sample ZZ2-19A) (Fig. 10a). In the Nb–Zr–Y triangular diagram (after Meschade, 1986) for basaltic rocks (Fig. 10b), they fall in the fields of within-plate alkali basalt ('AI' in the figure) and within-plate tholeiite/alkali basalt ('AII' in the figure). The Y–La–Nb triangular diagram (after Cabanis and Lecolle, 1989) for basaltic rocks (Fig. 10c) suggests continental basalt ('2A' in the figure) and alkali basalt from intercontinental rift ('3A' in the figure). The published geochemical data (Munyanyiwa et al., 1997) also fall in the fields of MORB, ocean-island, island arc, continent, or within-plate in Fig. 10c.

In the Th/Yb versus Nb/Yb binary plot (Fig. 10d; after Pearce, 2008), one mafic orthogneiss (sample ZZ2-14A) is plotting away from the non-arc mantle array, suggesting subduction-zone flux or input of a crustal component. Another mafic orthogneiss (sample ZZ2-19A) is plotting along the non-arc mantle array. This rock might have been derived from an oceanic-island basalt (OIB) component, which is also consistent with the discrimination based on the TiO_2–MnO–P_2O_5 triangular diagram (Fig. 10a).

4.4. P-T conditions

4.4.1. Geothermobarometer

We applied several geothermobarometers to orthogneisses to obtained peak metamorphic conditions of the study area, and compared the results with available *P-T* data from the Zambezi Belt. The garnet-hornblende geothermometer was applied to an equilibrium assemblage of garnet and hornblende in a meta-ultramafic rock (sample ZZ2-12) from the Allochthonous Terrain. The estimated temperature range for the garnet-hornblende pairs is 640–670 °C based on the method of Graham and Powel (1984). The application of the method of Ravna (2000) gave nearly consistent temperatures of 650–690 °C. The metamorphic pressure for the meta-ultramafic rock was calculated using Al-in-hornblende geobarometer of Hammarstrom and Zen (1986) as 9.8–9.9 kbar. The application of the method of Schmidt (1992) gave nearly consistent pressure range of 10.0–10.1 kbar. On the other hand, calculated metamorphic pressures for mafic orthogneiss (sample ZZ2-14A, Allochthonous Terrain) and felsic orthogneisses (samples ZZ1-3C and ZZ1-10A, Marginal Gneiss Terrain) based on the method of Hammarstrom and Zen (1986) are lower; 6.4–8.1 kbar,

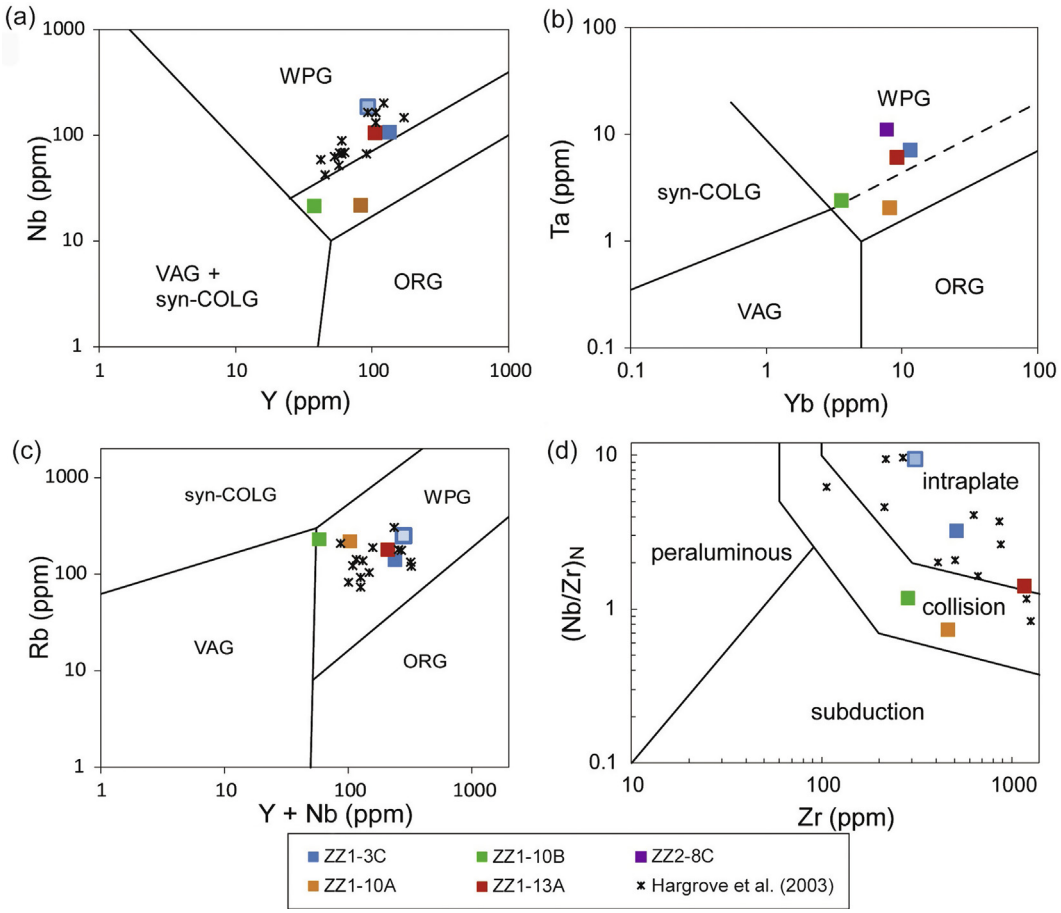

Figure 9. Discrimination diagrams for felsic orthogneisses from the Zambezi Belt based on minor elements. (a) Nb–Y diagram (after Pearce et al., 1984). (b) Ta–Yb diagram (after Pearce et al., 1984). (c) Rb–(Y + Nb) diagram (after Pearce et al., 1984). VAG: volcanic-arc granites, syn-COLG: syn-collisional granites, WPG: within plate granites, ORG: ocean-ridge granites. (d) $(Nb/Zr)_N$–Zr diagram (after Thiéblemont and Tegyey, 1994; Thiéblemont, 1999). Available geochemical data of felsic orthogneisses from the Zambezi Belt in northern Zimbabwe (after Hargrove et al., 2003) are also plotted in (a), (c), and (d) for comparison.

6.8–6.9 kbar, and 8.8–9.3 kbar, respectively. Application of the method of Schmidt (1992) gave slightly higher-pressure conditions (6.7–8.4 kbar, 7.1–7.2 kbar, and 9.0–9.5 kbar, respectively) for the samples. The metamorphic pressure for the mafic orthogneiss (sample ZZ2-14A, Allochthonous Terrain) was also calculated using garnet-hornblende-plagioclase-quartz geobarometer of Kohn and Spear (1990), and high-pressure conditions of 9.4–10.7 kbar (at 700 °C) were obtained.

Metamorphic temperatures were also estimated using hornblende-plagioclase geothermometry as the two minerals commonly coexist in many mafic and felsic orthogneiss samples. Holland and Blundy (1994) calibrated two geothermometers based on hornblende solid solution models and well-constrained natural and experimental studies. The edenite-richterite reaction is applicable to both quartz-bearing and quartz-free rocks and the edenite-tremolite reaction is applicable to quartz-bearing rocks. As quartz is absent in mafic orthogneiss (sample ZZ2-14A, Allochthonous Terrain), we adopted the edenite-richterite method and obtained temperatures of 780–845 °C at 7 kbar for the mafic orthogneiss. Application of methods on the assemblage in felsic orthogneiss (samples ZZ1-3C and ZZ1-10A, Marginal Gneiss Terrain) yielded lower-temperature ranges of 690–770 °C and 710–820 °C, respectively, at 7 kbar.

Based on the results of geothermobarometry, we obtained *P-T* conditions of 700–780 °C/6.7–7.2 kbar (sample ZZ1-3C), 680–800 °C/8.8–9.5 kbar (sample ZZ1-10A), 650–690 °C/9.8–10.1 kbar (ZZ2-12), and 800–875 °C/10–11 kbar (sample ZZ2-14A).

4.4.2. Phase equilibrium modeling

We also attempted to estimate *P-T* conditions of the stability of mineral assemblages in orthogneisses from the Zambezi Belt using THERMOCALC 3.45 (Powell and Holland,1988; Holland and Powell, 1998, 2011; data set tcds62, file created February 2012) for evaluating the results of geothermobarometry. The pseudo-section calculations were undertaken in the system Na_2O-CaO-K_2O-FeO-MgO-Al_2O_3-SiO_2-H_2O-TiO_2-Fe_2O_3 (NCKFMASHTO), because it is probably the most suitable approximation to model the felsic to mafic orthogneisses examined in this study. However, we failed to constrain peak *P-T* conditions for felsic orthogneisses probably because of simple mineral assemblages in orthogneiss samples, due to which the obtained *P-T* fields are too large. We could obtain a reasonable pseudosection for one meta-ultramafic rock (sample ZZ2-12) from the Allochthonous Terrain as summarized below.

The phases and their activity-composition models considered in the modeling are tonalitic (metabasite) melt and clinoamphibole (Green et al., 2016), garnet, biotite, muscovite, and chlorite (White et al., 2014), epidote (Holland and Powell, 2011), feldspars (Holland and Powell, 2003), spinel-magnetite (White et al., 2002), and ilmenite-hematite (White et al., 2000). Quartz, rutile, and H_2O are

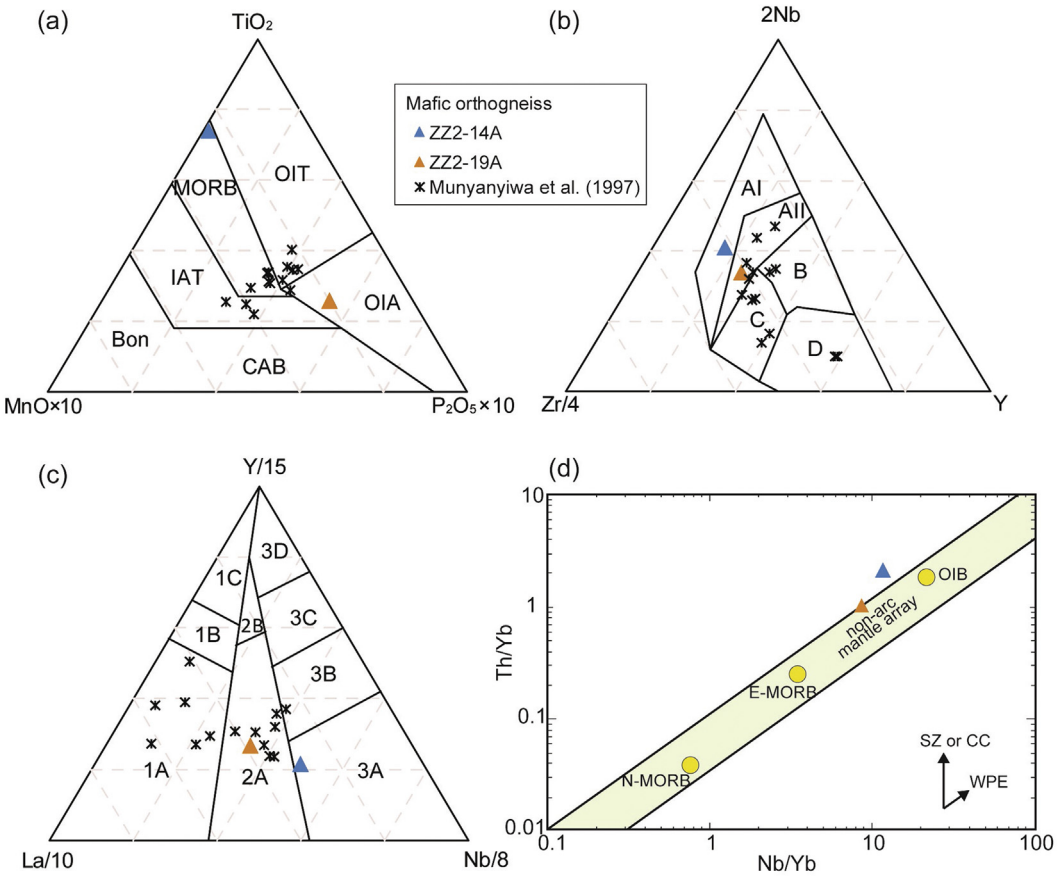

Figure 10. Discrimination diagrams showing compositions of mafic orthogneisses from the Zambezi Belt. (a) TiO_2–MnO × 10–P_2O_5 × 10 diagram (after Mullen, 1983). CAB: (island-arc) calc-alkaline basalt, IAT: island arc tholeiite, MORB: mid ocean ridge (and marginal basin) basalt, OIT: ocean island tholeiite, OIA: ocean island alkalic basalt, Bon: boninite. (b) 2Nb–Zr/4–Y diagram (after Meschede, 1986). AI: within-plate alkali basalt, AII: within-plate tholeiite and within-plate alkali basalt, B: P-type MORB, C: within-plate tholeiite and volcanic arc basalt, D: volcanic arc basalt and N-type MORB. (c) Y/15–La/10–Nb/8 diagram (after Cabanis and Lecolle, 1989). 1A: calc-alkali basalt, 1C: volcanic arc tholeiite, 1B: an area of overlap between 1A and 1C, 2A: continental basalt, 2B: back-arc basin basalt, 3A: alkali basalt from intercontinental rift, 3B: enriched E-MORB, 3C: weakly enriched E-MORB, 3D: N-MORB. (d) Th/Yb versus Nb/Yb plot showing the petrogenetic character of mafic orthogneisses from the Zambezi Belt (after Pearce, 2008). SZ: subduction-zone flux, CC: crustal contamination vector, WPE: within-plate enrichment, N-MORB: normal mid-oceanic ridge basalt, E-MORB: enriched mid-oceanic ridge basalt, OIB: ocean island basalt. N-MORB, E-MORB, and OIB are from Sun and McDonough (1989). Available geochemical data of mafic orthogneisses from the Zambezi Belt in northern Zimbabwe (after Munyanyiwa et al., 1997) are also plotted in (a), (b), and (c) for comparison.

treated as pure phases. The chemical composition (in wt.%) of the sample is SiO_2 = 30.53, Al_2O_3 = 15.11, Fe_2O_3 = 11.17, FeO = 22.10, MgO = 5.78, CaO = 5.45, Na_2O = 0.86, K_2O = 0.16, TiO_2 = 5.71. MnO was ignored in the modeling because of its low concentration. FeO/Fe_2O_3 ratio was determined by titration. Water content of the rock is not known, therefore we evaluated H_2O content using *T* versus mole H_2O diagrams (not shown) and adopted relatively high H_2O content of 5.0 mol.% because the peak mineral assemblage in the rock was not stable at H_2O < 5.0 mol.%.

Fig. 11 shows a *P-T* pseudosection for sample ZZ2-12 which contains the peak mineral assemblage of garnet + hornblende + ilmenite ± H_2O. The stability field of the peak assemblage plotted in the pseudosection suggests a *P-T* range of 625–750 °C and 6.5–9.3 kbar (area PK in Fig. 11). The condition is nearly consistent with that from geothermobarometry (640–670 °C and 9.8–10.1 kbar), although the pressure condition is slightly lower.

4.5. Zircon U-Pb geochronology

The results of zircon U-Pb analyses of felsic orthogneisses (samples ZZ1-3C and ZZ1-10B), pelitic schist (sample ZZ2-7A), and felsic paragneisses (samples ZZ2-21 and ZZ2-22) are given in Supplementary Table 7. CL images of representative zircons are shown in Fig. 12 together with analyzed spots and ages. Concordia diagrams and probability density diagrams with histograms of ages are shown in Fig. 13. In the following text and figures, ages older or younger than 1.0 Ga are discussed based on $^{207}Pb/^{206}Pb$ or $^{206}Pb/^{238}U$ ages, respectively. The error levels are 1-σ. The data processing was carried out using the Isoplot 4.15 software (Ludwig, 2008).

4.5.1. Felsic orthogneiss

Zircon grains from sample ZZ1-3C are translucent, colorless or light brownish, subidioblastic, and partly rounded in habit (Fig. 12a). The grains show a size range of 40–460 μm and an aspect ratio of 4:1 to 2:1. In CL images, most of the grains show oscillatory-zoned (grain 60) or homogeneous textures (grain 71), and a few grains show structureless internal domains and very thin rims. 101 spots were analyzed from 61 grains with 49 spots showing <10% discordance. The results show that spot ages from the grains with <10% discordance vary from 861 ± 14 Ma to 543 ± 8 Ma ($^{206}Pb/^{238}U$ age). Their Th and U contents and Th/U ratio show wide ranges of 0–940 ppm, 93–1682 ppm, and 0–2.17, respectively. The histogram

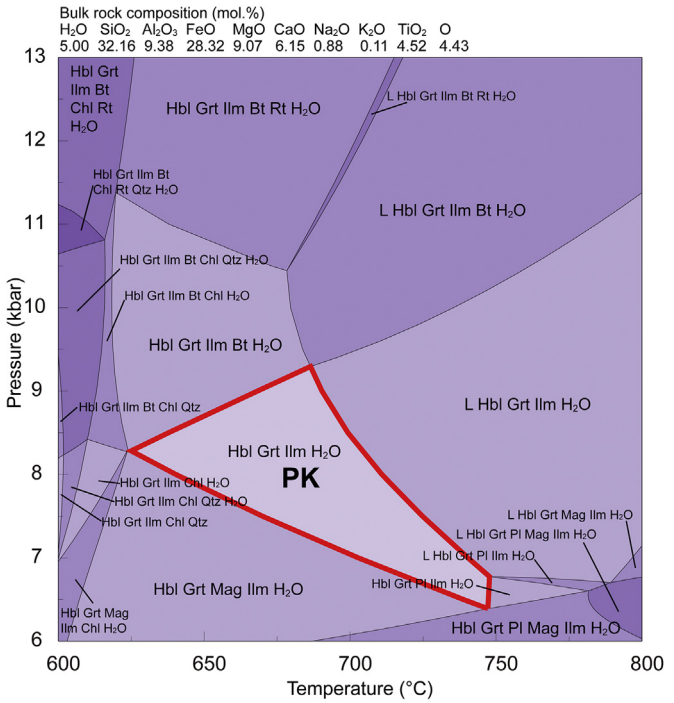

Figure 11. *P-T* diagram showing calculated pseudosection of peak (PK) mineral assemblages in meta-ultramafic rock from the Allochthonous Gneiss Terrain (sample ZZ2-12). L: inferred melt, Hbl: hornblende, Grt: garnet, Pl: plagioclase, Mag: magnetite, Ilm: ilmenite, Bt: biotite, Chl: chlorite, Rt: rutile, Qtz: quartz.

indicates the highest peak with weighted mean $^{206}Pb/^{238}U$ age of 813 ± 5 Ma (MSWD = 0.36, n = 12). Their Th/U ratios are distributed from 0.42 to 0.85, suggesting a magmatic origin. The youngest peak shows a weighted mean $^{206}Pb/^{238}U$ age of 555 ± 20 Ma (MSWD = 2.6, n = 4), and such young zircon data are further divided into two groups; three low-Th/U (0.004–0.1) and one high-Th/U (0.4) grains. The former group with 543 ± 9 Ma (spot 16-2), 550 ± 9 Ma (spot 30-2), and 576 ± 9 Ma (spot 49) zircons can be regarded as metamorphic in origin because zircons with low Th/U ratios of <0.1 have been regarded as metamorphic (e.g., Williams and Claesson, 1987; Kinny et al., 1990; Maas et al., 1992). Although the latter 552 ± 6 Ma zircon (spot 71-2) could be a relict magmatic grain because of high-Th/U ratio (0.4), its occurrence as a homogeneous rim suggest the zircon was also formed during high-grade metamorphism.

Zircon grains from sample ZZ1-10B are translucent, colorless or light brownish, and show subidioblastic and partly rounded or irregular shape (Fig. 12b). They show a size range of 30–430 μm and an aspect ratio of 4:1 to 1.3:1. In CL images, most of the grains show oscillatory-zoned (grain 22) or structureless cores surrounded by bright and very thin rims. 66 spots were analyzed from 56 grains and the ages of 11 spots with <10% discordance vary from 2887 ± 13 Ma to 2619 ± 14 Ma ($^{207}Pb/^{206}Pb$ age). Their Th and U contents and Th/U ratio show ranges of 94–285 ppm, 172–438 ppm, and 0.38–0.93, respectively. Most of concordant ages of cores are distributed from 2603 ± 17 Ma to 2706 ± 16 Ma with weighted mean $^{207}Pb/^{206}Pb$ age of 2655 ± 21 Ma (MSWD = 3.8, n = 10) (Fig. 13c and d). Their high-Th/U ratios scattering from 0.38 to 0.93 suggest their magmatic origin. The plots of >10% discordance ages are aligned along a discordia, probably suggesting Neoarchean crystallization and early Cambrian high-grade metamorphism.

4.5.2. Pelitic schist

Zircon grains from sample ZZ2-7A are translucent, colorless or light brownish, and subidioblastic and partly rounded in habit (Fig. 12c). The grains show a size range of 40–310 μm and an aspect ratio of 4:1 to 1:1. In CL images, most of the grains display oscillatory-zoned (grain 63), irregular concentric-zoned (grain 107), or structureless cores mantled by bright rim (grain 74). 173 spots were analyzed from 134 zircon grains with 105 spots showing <10% discordance. The results show that spot ages from the grains with <10% discordance exhibit a wide age range of 2702 ± 17 Ma ($^{207}Pb/^{206}Pb$ age) to 627 ± 6 Ma ($^{206}Pb/^{238}U$ age) (Fig. 13e and f), implying multiple sources and various provenances of the rock. Their Th and U contents and Th/U ratio also exhibit wide ranges of 14–1035 ppm, 31–1270 ppm, and 0.08–1.60, respectively. They show four age populations: Neoarchean (2702 ± 17 Ma to 2643 ± 20 Ma, $^{207}Pb/^{206}Pb$ age), Paleoproterozoic (2189 ± 24 Ma to 1603 ± 49 Ma, $^{207}Pb/^{206}Pb$ age), Mesoproterozoic to early Neoproterozoic (1489 ± 49 Ma [$^{207}Pb/^{206}Pb$ age] to 859 ± 9 Ma [$^{206}Pb/^{238}U$ age]), and Neoproterozoic (754 ± 9 Ma to 627 ± 6 Ma, $^{206}Pb/^{238}U$ age), with dominant peaks of ca. 2670 Ma, 2150 Ma, 1990 Ma, 1870 Ma, and 1160 Ma. Although there is no systematic correlation between the ages and Th/U ratios, two spot ages from relatively homogeneous rim (grain 74) and core (grain 94-2) with lower Th/U ratios (0.08 and 0.11, respectively) yielded younger Neoproterozoic ages of 627 ± 6 Ma and 670 ± 10 Ma, respectively, possibly suggesting Neoproterozoic metamorphism.

4.5.3. Felsic paragneiss

Zircon grains from sample ZZ2-21 are translucent, colorless and unusually light brownish, and subidioblastic to partly rounded in habit (Fig. 12d). The grains show a size range of 25–170 μm and an aspect ratio of 4:1 to 1:1. In CL images, most of the grains display oscillatory-zoned (grain 7) or homogeneous textures (grain 6). 86 spots were analyzed from 60 zircon grains with 51 spots showing <10% discordance. The results show that spot ages from the grains with <10% discordance exhibit a wide age range of 2632 ± 29 Ma ($^{207}Pb/^{206}Pb$ age) to 514 ± 5 Ma ($^{206}Pb/^{238}U$ age), implying multiple sources and various provenances of the rock. Their Th and U contents and Th/U ratio show wide ranges of 5–524 ppm, 51–955 ppm, and 0.01–1.44, respectively. They show four age populations: Neoarchean (2632 ± 29 Ma, $^{207}Pb/^{206}Pb$ age), Paleoproterozoic (2098 ± 33 to 1715 ± 39 Ma, $^{207}Pb/^{206}Pb$ age), Mesoproterozoic to early Neoproterozoic (1590 ± 66 Ma [$^{207}Pb/^{206}Pb$ age] to 925 ± 10 Ma [$^{206}Pb/^{238}U$ age]), and Neoproterozoic (658 ± 8 Ma to 514 ± 5 Ma, $^{206}Pb/^{238}U$ age), with major age peaks of ca. 2630 Ma, 2000 Ma, 1810 Ma, 1380 Ma, 940 Ma, and 560 Ma (Fig. 13g and h). Most of concordant ages of cores are distributed from Neoarchean to early Neoproterozoic (2632 ± 29 Ma [$^{207}Pb/^{206}Pb$ age] to 925 ± 10 Ma [$^{206}Pb/^{238}U$ age]). On the other hand, $^{206}Pb/^{238}U$ ages of rims (seven spots) with low discordance (<10%) vary from 658 ± 8 Ma to 514 ± 5 Ma (see Fig. 13h), among which three spots with consistent ages of 553 ± 7 Ma, 556 ± 6 Ma, and 560 ± 6 Ma show a weighted mean age of 557 ± 7 Ma (MSWD = 0.3, n = 3). Th/U ratios of Neoarchean to early Neoproterozoic (2632–925 Ma) spots with <10% discordance vary from 0.12 to 1.44 (magmatic), whereas those of late Neoproterozoic spots are very low (<0.06), suggesting metamorphic overgrowth at 557 ± 7 Ma.

Zircon grains from sample ZZ2-22 are translucent, colorless or light brownish, and show subidioblastic, rounded, or irregular shape in habit (Fig. 12e). The grains show a size range of 20–200 μm and an aspect ratio of 4.2:1 to 1.3:1. In CL images, most of the grains show

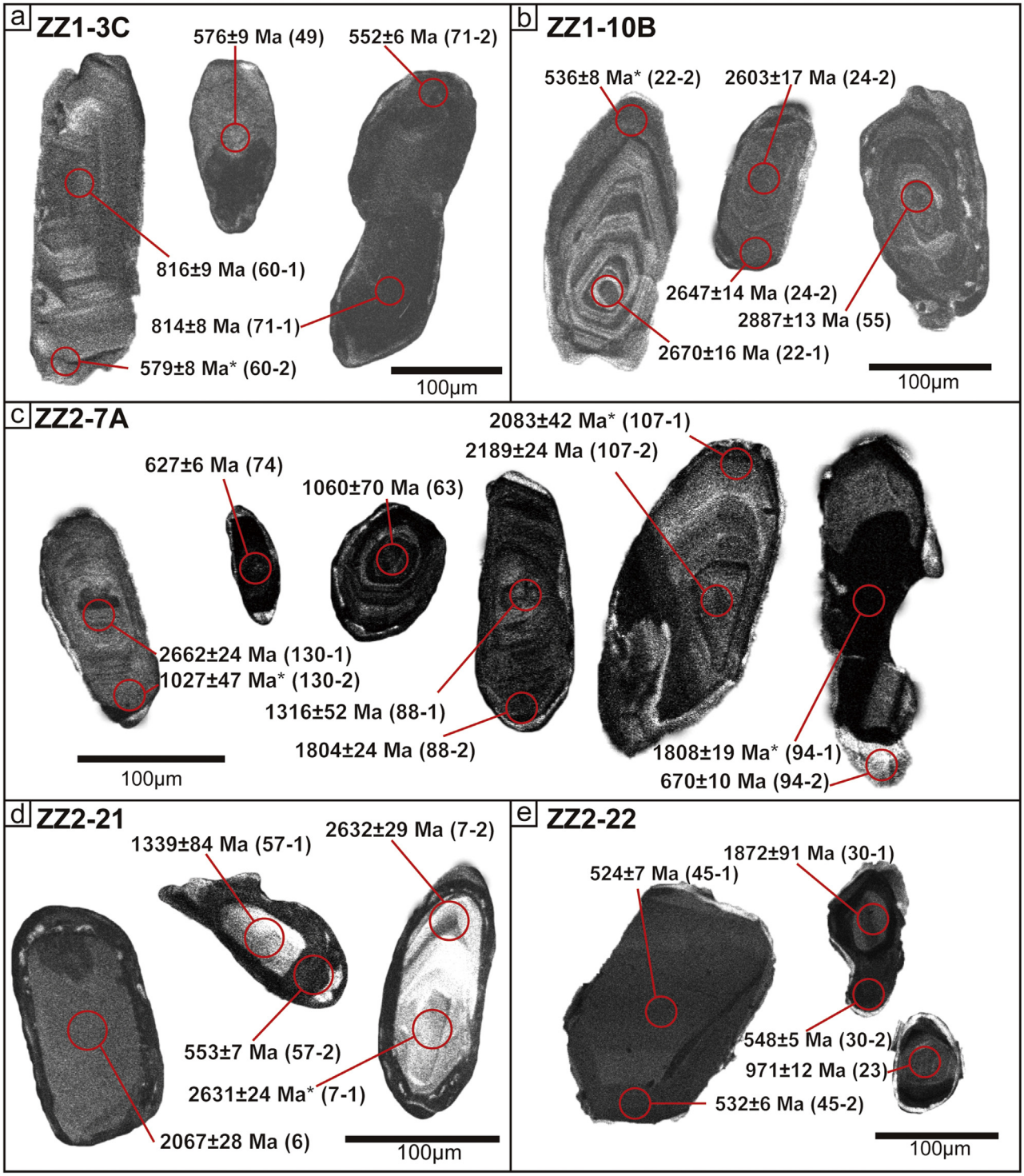

Figure 12. Cathodoluminescence (CL) images of zircon grains obtained from samples ZZ1-3C (a), ZZ1-10B (b), ZZ2-7A (c), ZZ2-21 (d), and ZZ2-22 (e). Red circles show the spots of U-Pb analysis with age value in Ma and spot number (parentheses). Ages older than 1.0 Ga are shown in $^{206}Pb/^{238}U$ age, whereas ages younger than 1.0 Ga are shown in $^{207}Pb/^{206}Pb$ age. Ages with asterisk indicate discordant (>10% discordance) data.

oscillatory-zoned (grain 30) or structureless core surrounded by bright and very thin rim (grain 45). 61 spots were analyzed from 56 grains with 14 spots showing <10% discordance, and the ages vary from 1872 ± 26 Ma ($^{207}Pb/^{206}Pb$ age) to 524 ± 7 Ma ($^{206}Pb/^{238}U$ age). Their Th and U contents and Th/U ratio show ranges of 146–619 ppm, 4–371 ppm, and 0.01–1.09, respectively. Most of the concordant ages of cores are early Neoproterozoic (927 ± 10 Ma to 1091 ± 91 Ma) with the highest peak at ca. 970 Ma (Fig. 13i and j). Their Th/U ratios show a range of 0.32–1.09, suggesting their magmatic origin. On the other hand, most of the spots on rims and homogeneous cores indicate late Neoproterozoic $^{206}Pb/^{238}U$ ages (with <10% concordance) ranging from 548 ± 5 Ma to 524 ± 7 Ma, and Th/U ratios of 0.01–0.06, based on which we infer zircon overgrowth during late Neoproterozoic to early Cambrian metamorphism.

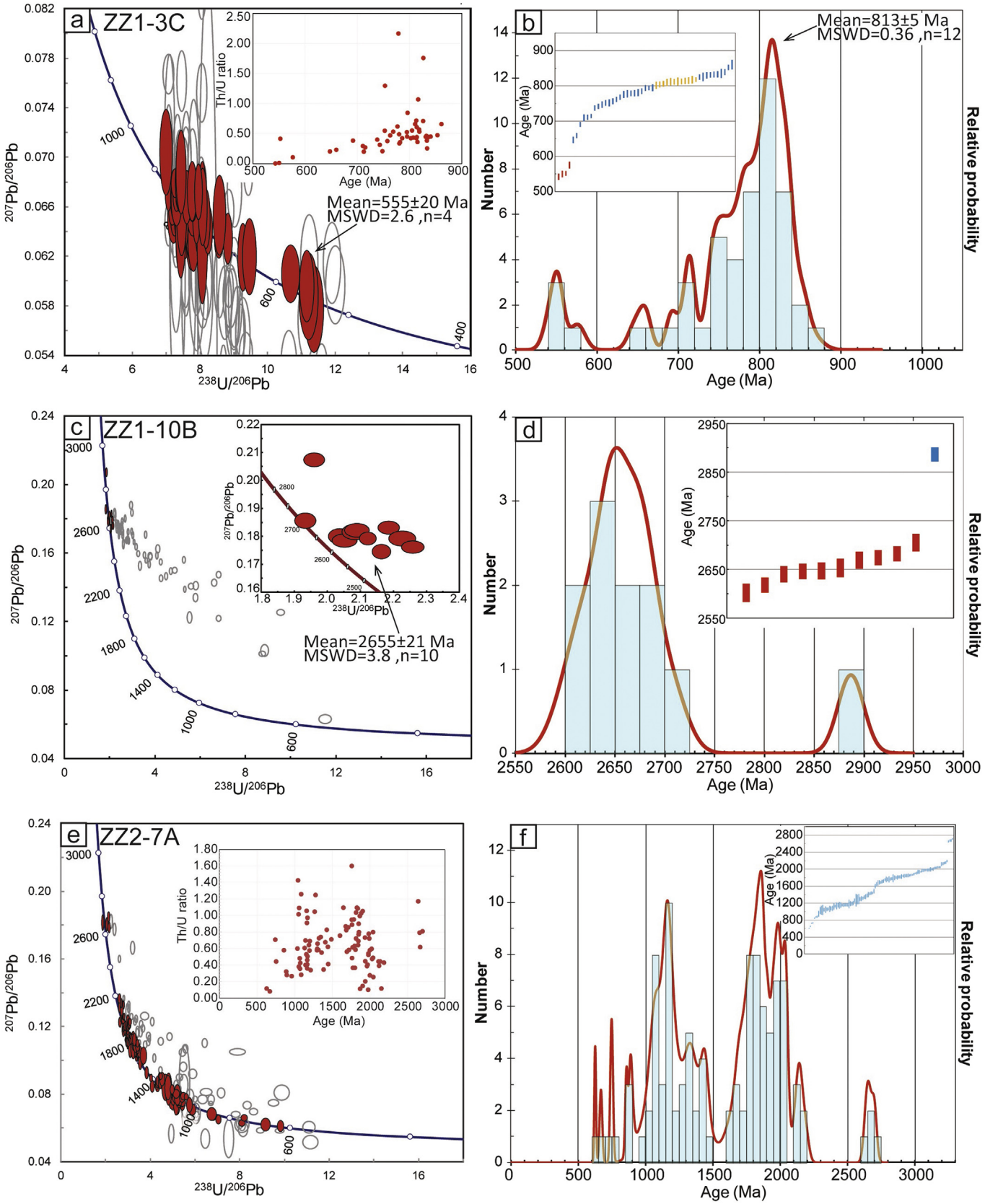

Figure 13. (a, c, e, g, and i) Tera-Wasserburg concordia diagrams and histograms with probability density plots of the samples from the Zambezi Belt in Zimbabwe. Red and grey circles in concordia diagrams imply concordant (<10% discordance) and discordant (>10% discordance) data, respectively. Inset figures exhibit Th/U ratio versus age in Ma. (b, d, f, h, and j) Histograms with probability density plots of concordant (<10% discordance) analyzed spots in our samples. Histograms show only concordant data. Ages older than 1.0 Ga are shown in $^{207}Pb/^{206}Pb$ age, whereas ages younger than 1.0 Ga are shown in $^{206}Pb/^{238}U$ age. Inset figures show the weighted mean age plots. Filled red and orange rectangles represent the data selected to calculate mean age, filled blue rectangles represent the other data.

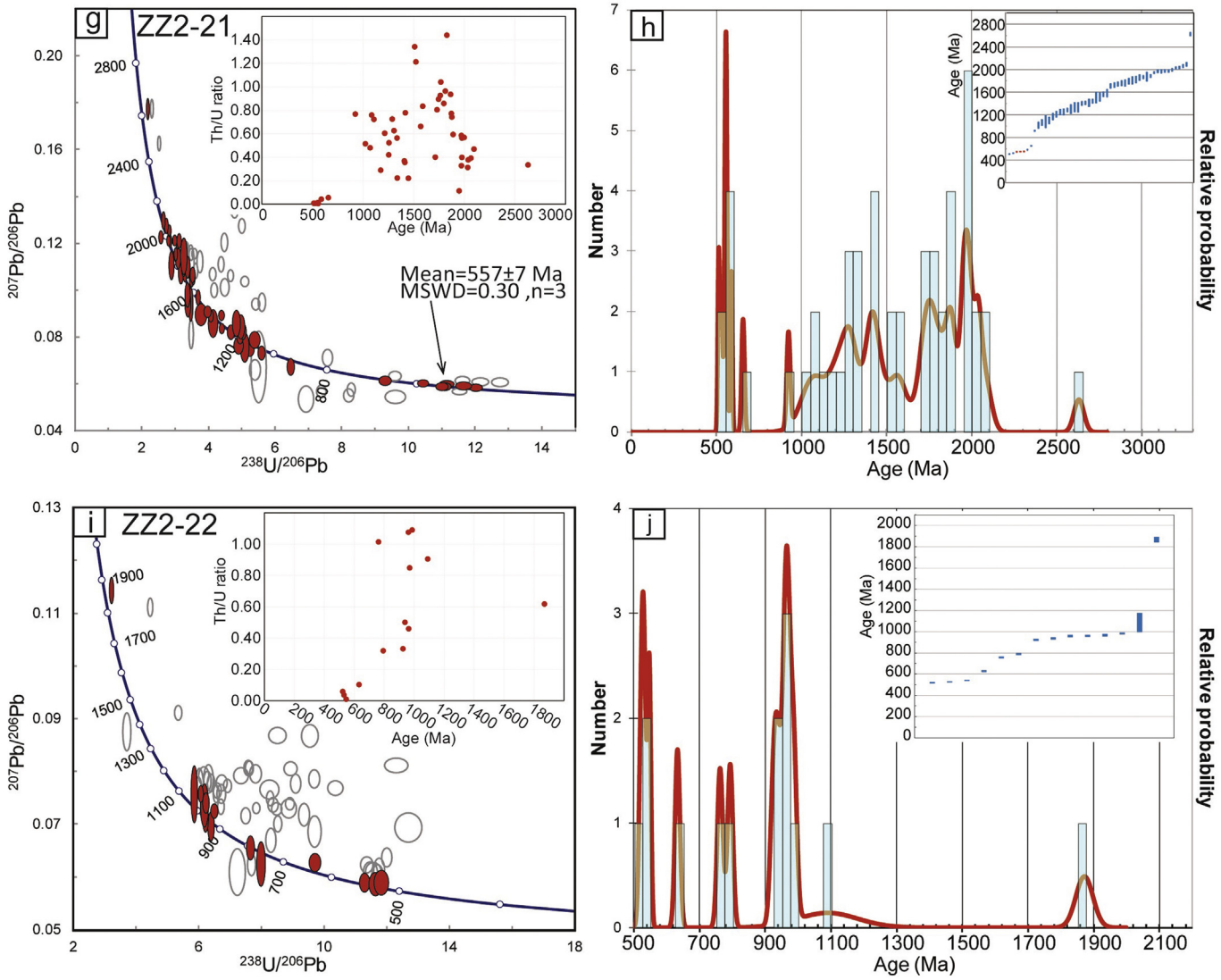

Figure 13. (*continued*)

5. Discussion

5.1. Petrology and geochemistry

Systematic petrological, geochemical, and zircon U-Pb geochronological data of felsic to mafic orthogneisses, meta-ultramafic rocks, and metasediments from the Zambezi Belt indicate Neoarchean (2655 Ma) and Early Neoproterozoic (813 Ma) magmatism, and latest Neoproterozoic (557–555 Ma) high-grade metamorphism in this region. These rocks are composed of meta-igneous mineral assemblages such as quartz + plagioclase + microcline + biotite ± calcic amphibole ± garnet ± titanite ± epidote ± muscovite (felsic orthogneiss; e.g., samples ZZ1-3C, ZZ1-10A, ZZ1-10B, ZZ1-13A, and ZZ2-8C), plagioclase + calcic amphibole + biotite ± garnet ± titanite ± quartz (mafic orthogneiss; e.g., samples ZZ2-14A and ZZ2-19A), calcic amphibole + plagioclase + orthopyroxene + cummingtonite + spinel + magnetite + garnet (metapyroxenite; e.g., sample ZZ2-15A), and garnet + calcic amphibole + magnetite + ilmenite (meta-ultramafic rock; e.g., sample ZZ2-12). Felsic orthogneiss occurs as the dominant lithology in many localities in the Marginal Gneiss Terrain, whereas mafic and meta-ultramafic rocks are dominant in the Allochthonous Terrain. The Marginal Gneiss Terrain also contains metasediments such as pelitic schist (quartz + muscovite + microcline + plagioclase + biotite; e.g., sample ZZ2-7A) and felsic paragneiss (quartz + plagioclase + biotite; e.g., samples ZZ2-21 and ZZ2-22).

Application of several geothermobarometers for felsic orthogneisses yielded upper amphibolite- to lower granulite-facies conditions of 680–800 °C and 6.7–9.5 kbar (700–780 °C/6.7–7.2 kbar for sample ZZ1-3C and 680–800 °C/8.8–9.5 kbar for sample ZZ1-10A) from the Marginal Gneiss Terrain. On the other hand, mafic orthogneiss sample ZZ2-14A from the Allochthonous Terrain yielded higher-grade conditions of 800–875 °C and 10–11 kbar, whereas lower temperature conditions of 650–690 °C and 9.8–10.1 kbar were obtained from meta-ultramafic rock (sample ZZ2-12) based on geothermobarometry and phase equilibria modeling. Hargrove et al. (2003) previously obtained metamorphic *P-T* condition of 610–670 °C/9.3–10.4 kbar for the Marginal Gneiss Terrain, and higher conditions of 890–920 °C/10–11 kbar for the

Allochthonous Terrain, which is consistent with the results of this study. As shown in Fig. 2b, these results indicate significant *P-T* variation within the study area. Such *P-T* variation suggests that the Zambezi Belt might correspond to a suture zone, and it is composed of several crustal blocks with different *P-T* evolution. This hypothesis is consistent with previous structural observations that the high-pressure Allochthonous Terrain structurally overlies the low-pressure Marginal Gneiss Terrain (Dirks and Jelsma, 2006).

The geochemical data of felsic orthogneisses show distinct features for the Neoarchean and Early Neoproterozoic igneous protoliths. The REE and trace element patterns as well as Nb–Y, Ta–Yb, and Rb–(Y + Nb) diagrams (Fig. 9) of felsic orthogneiss from the Marginal Gneiss Terrain (samples ZZ1-3C, ZZ1-10A, ZZ1-10B, ZZ1-13A, and ZZ2-8C) suggest that the protoliths of these rocks were derived from within-plate affinity, and $(Nb/Zr)_N$–Zr diagram (Fig. 10d) suggests collision or intraplate-related origin, which are consistent with the results of previous geochemical studies from the Marginal Gneiss Terrain (e.g., Hargrove et al., 2003). A mafic orthogneiss from the Marginal Gneiss Terrain (sample ZZ2-19A) shows mid-oceanic ridge basalt, within-plate basalt, or intercontinental rift basalt affinities based on various discrimination diagrams (Fig. 10). A mafic orthogneiss from the Allochthonous Terrain (sample ZZ2-14A) also shows a non-arc signature such as ocean-island, seamount, or continental basalts. A similar signature has been reported for amphibolites from the Makuti Group of the western part of the Zambezi Belt (Munyanyiwa et al., 1997). All these geochemical data suggest that the Zambezi Belt is composed of meta-granitic rocks with continental rift origin along with various non-arc related mafic rocks, which were assembled before the latest Neoproterozoic final collision.

5.2. Zircon U-Pb geochronology

5.2.1. Magmatic zircon

The morphology, oscillatory zoning with core-rim texture from CL images (Fig. 12), and high Th/U ratio of zircon grains in the felsic orthogneiss suggest that the dominant zircon population preserves magmatic crystallization history. The weighted mean $^{206}Pb/^{238}U$ age of 813 ± 5 Ma from sample ZZ1-3C suggests early Neoproterozoic emplacement of felsic magma through within-plate magmatism possibly associated with intra-continental rifting (e.g., Munyanyiwa et al., 1997; Hanson et al., 1998; Vinyu et al., 1999; Hargrove et al., 2003; John et al., 2004). Such early Neoproterozoic magmatic event has been reported in previous studies (e.g., Hanson et al., 1988b, 1998; Barton et al., 1991; Dirks et al., 1999; Vinyu et al., 1999; Hargrove et al., 2003). For example, Vinyu et al. (1999) reported zircon and titanite U-Pb ages of ca. 870–850 Ma as a protolith age. Hargrove et al. (2003) also argued protolith crystallization age of 795 ± 2 Ma using IDTIMS. The magmatism might be associated with the break-up of Rodinia supercontinent at ca. 880 Ma (e.g., Porada and Berhorst, 2000; John et al., 2003; Johnson et al., 2007).

The zircon U-Pb ages of magmatic grains from sample ZZ1-10B vary from 2887 ± 13 Ma to 2619 ± 14 Ma. The weighted mean $^{207}Pb/^{206}Pb$ age of 2655 ± 21 Ma and geochemical data suggest that the Neoarchean emplacement of the protolith magma could be related to within-plate magmatism. The older 2887 Ma zircon was probably trapped as a xenocryst during the intrusion of 2655 Ma felsic magma, suggesting reworking of ca. 2.9 Ga continental crust through Neoarchean continental rifting. The results are comparable with the previous geochronological data of Johnson et al. (2007) that reported a 2681 ± 9 Ma magmatic event in the Zambezi Belt. Such Neoarchean event might be correlated with the 2.7–2.6 Ga thermal events throughout the Zimbabwe Craton (such as the intrusion of Chilimanzi suite granitoids), which has been regarded as reworking of the craton.

5.2.2. Detrital zircon

Cores of detrital zircon grains in a pelitic schist sample (ZZ2-7A) exhibit a wide age range from Neoarchean to Neoproterozoic (ca. 2700–745 Ma) with major age peaks of ca. 2650, 2150, 2000, 1860, and 1150 Ma, and minor peaks of ca. 880 Ma and 750 Ma (Fig. 13f). The felsic paragneiss samples (ZZ2-21 and ZZ2-22) also contain Neoarchean to Neoproterozoic (ca. 2630–925 Ma) detrital zircon cores, yielding three dominant age populations of Neoarchean (ca. 2630 Ma), Paleoproterozoic (ca. 2100–1700 Ma), and Mesoproterozoic to early Neoproterozoic (ca. 1600–920 Ma) with major peaks of ca. 2650, 2000, 1810, 1380, 1430, and 940 Ma (Fig. 13h, j). The results of this study suggest that the metasediments of the Zambezi Belt were dominantly derived from Neoarchean (ca. 2700–2630 Ma), Paleoproterozoic (ca. 2200–1700 Ma), Mesoproterozoic (ca. 1500–950 Ma), and early Neoproterozoic (ca. 900–750 Ma) terranes.

Neoarchean basement rocks are reported from several crustal blocks in southern Africa such as the Sesombi suite (ca. 2700 Ma), the Wedza suite (ca. 2650 Ma), the Chilimanzi suite (ca. 2600 Ma) in the Zimbabwe Craton (Wilson et al., 1995), the Tanzania Craton (ca. 2850–2620 Ma, with the peak crustal growth at ca. 2700–2650 Ma: Kabete et al., 2012; Thomas et al., 2013, 2016; Sanislav et al., 2014), and the Congo-Kasai Craton (ca. 2680–2600 Ma: Delhal et al., 1976; Cahen et al., 1984; Caen-Vahette et al., 1988; Tchameni et al., 2000; Batumike et al., 2009). The zircon ages of these cratons are comparable with the Neoarchean (ca. 2700–2630 Ma) detrital zircons in the Zambezi Belt. The Zimbabwe Craton could be the main source of the Neoarchean zircon because of its proximal location.

Paleoproterozoic rocks have been reported from the Ubendian-Usagaran Belt in Tanzania (ca. 2100–1900 Ma: Lenoir et al., 1994; Ring et al., 1997; Collins et al., 2004), the Bangweulu Block in Zambia (ca. 2000–1800 Ma: De Waele et al., 2003a), the Magondi Belt in Zimbabwe (ca. 2000–1930 Ma: Munyanyiwa et al., 1995; Majaule et al., 2001; McCourt et al., 2001), and the northern part of the Damara Belt in Namibia (2050–1660 Ma: Burger et al., 1976; Tegtmeyer and Kröner, 1985; Seth et al., 1998; Franz et al., 1999; Luft et al., 2001; Singletary et al., 2003). The zircon age spectra of these regions are comparable with ca. 2200–1700 Ma zircons in the Zambezi metasediments, and suggest that the Magondi Belt and the Bangweulu Block could be the main and proximal sources of the Paleoproterozoic zircons.

Mesoproterozoic rocks have been reported from the Choma-Kalomo Block (ca. 1370 Ma and 1180 Ma: Hanson et al., 1988a; Bulambo et al., 2004, 2006), the Nampula Complex in Mozambique (ca. 1150–1030 Ma: Costa et al., 1994; Kröner et al., 1997; Grantham et al., 2008), the Irumide Belt in Zambia (ca. 1050–1000 Ma, 950 Ma: De Waele et al., 2006a,b), the southern Irumide Belt (ca. 1100–1020 Ma, 930 Ma: Goscombe et al., 2000; Johnson et al., 2006; Mänttäri, 2008), and the Maud Belt in East Antarctica (ca. 1170–1050 Ma: Arndt et al., 1991; Jacobs et al., 1998, 2003; Paulsson and Austrheim, 2003; Board et al., 2004; Bisnath et al., 2006). Among the above possible sources, the Choma-Kalomo Block could be a proximal source for the Mesoproterozoic (ca. 1500–950 Ma) zircons of the Zambezi Belt.

There are several Early Neoproterozoic terranes around the Zambezi Belt such as the Mwashia Group in the Lufilian Belt (ca. ~765 Ma, Key et al., 2001), the Nchanga Granite in the Lufilian Belt (ca. 883 Ma, Armstrong et al., 2005), the Ubendian shear belt in Tanzania (ca. 724 Ma, Lenoir et al., 1994), and orthogneiss blocks in the Mozambique Belt (ca. 870–780 Ma, Mänttäri, 2008). These rocks could be sources of the early Neoproterozoic (ca. 900–750

Ma) detrital zircons in the Zambezi Belt, although we infer that the Lufilian Belt could be a dominant and proximal source of the zircons.

We also evaluated minor peaks (ca. 2150, 1600, 1350, and 1100 Ma) in the probability density plots (Fig. 13f, j) and inferred the provenances of the zircons. For example, Middle Paleoproterozoic (ca. 2150 Ma) ages have been reported from the Dete-Kamativi Inlier in Magondi Belt (ca. 2020–2150 Ma: Priem et al., 1971; Glynn et al., 2015; Master et al., 2015), the Bangweulu Block in Zambia (ca. 2160–2100 Ma: De Waele et al., 2003a), and the Ubendian-Usagaran Belt of Malawi (ca. 2200–2050 Ma: Ring et al., 1997), whereas Late Paleoproterozoic (ca. 1600 Ma) ages have been obtained from the Lukamfwa suite of the Irumide Belt (ca. 1660–1550 Ma: De Waele et al., 2003b, 2006b). Mesoproterozoic (ca. 1350 and 1100 Ma) zircons might have been derived from the Umkondo Igneous Province in Botswana (ca. 1100 Ma: Schwartz et al., 1996; Kampunzu et al., 2000; Singletary et al., 2003; de Kock et al., 2014), and the Kibaran Belt (ca. 1380–1350 Ma: Deblond et al., 2001; Tack et al., 2002; Kokonyangi et al., 2004). The Paleoproterozoic to Early Neoproterozoic detrital zircons have been obtained from both the northern and the southern part of the Zambezi Belt. We thus conclude that all the detrital zircons in the Zambezi Belt have appropriate provenances in the adjacent Kalahari and Congo Cratons, although the Kalahari Craton could be a proximal source of most of the zircons.

5.2.3. Metamorphic zircon

The ages of structureless zircon grains and homogeneous rims around inherited/magmatic cores can be regarded as the timing of metamorphism (Corfu et al., 2003). Most of them in our samples with <10% discordance age display late Neoproterozoic to early Cambrian ages (670–514 Ma) (Fig. 13) with weighted mean ages of 555 ± 20 Ma (sample ZZ1-3C, felsic orthogneiss) and 557 ± 7 Ma (sample ZZ2-21, felsic paragneiss). The analyzed spots show lower Th/U ratios of 0.01–0.06 than those of magmatic and detrital cores (Th/U > 0.12), which further confirms that the 557–555 Ma thermal event probably corresponds to peak metamorphism. The results suggest that metamorphism of the Zambezi Belt took place during late Neoproterozoic to early Cambrian, which is consistent with the results of previous studies that reported similar metamorphic ages (ca. 560–530 Ma) from various lithologies in the belt (e.g., Barton et al., 1991, 1993; Mariga et al., 1998; Hargrove et al., 2003; John et al., 2004; Johnson et al., 2007). These ages might correspond to the final collisional event of the Kalahari and Congo Cratons associated with the Kuunga Orogen (570–530 Ma: Meert et al., 1995; Meert and Lieberman, 2008). However, the metasediments in the Zambezi Belt also contain several zircons showing slightly older metamorphic ages of 670–627 Ma, suggesting Cryogenian thermal events before the 557–555 Ma final collision. Kawakami et al. (2016) reported similar Cryogenian metamorphic ages of 650–580 Ma from the Lützow-Holm Complex in East Antarctica in the eastern part of the Kuunga Orogen, and inferred that the area underwent polymetamorphism. Ca. 650 Ma metamorphic ages have also been reported from latest Neoproterozoic suture zones in India and Sri Lanka (e.g., Koizumi et al., 2014; Takamura et al., 2015), which corresponds to parts of the Kuunga Orogen. Such 670–627 Ma metamorphism inferred in this study might be related to collision of magmatic arcs or microcontinents before the final collision, although further petrological, geochemical, and geochronological investigations are necessary to argue the nature of the Cryogenian thermal event in the Zambezi Belt.

Generally, metamorphic ages recorded in zircons within metasediments are regarded as the minimum depositional age of protolith sediments (e.g., Nelson, 2001). Therefore, the protolith sediments of the Zambezi Belt probably deposited before the late Neoproterozoic (670–627 Ma) thermal event. As sample ZZ2-7A contains the youngest detrital zircon of 744 ± 9 Ma with high Th/U ratios of 0.71, the depositional age of the protolith sediments can be constrained between 744 Ma and 670 Ma.

5.3. Correlation of detrital zircons with other orogenic belts

Many detrital zircon ages have been published from adjacent Neoproterozoic–Cambrian orogens such as the Mozambique Belt, Damara Belt, and southern Madagascar (e.g., Mänttäri, 2008; Bingen et al., 2009; Thomas et al., 2010; Collins et al., 2012; Boger et al., 2014; Foster et al., 2015) (see Fig. 14). We thus compare detrital zircon ages from the Zambezi Belt with those from the adjacent orogenic belts. The Damara Belt contains Neoarchean detrital zircons (ca. 2700–2450 Ma, Foster et al., 2015) similar to our ca. 2700–2630 Ma zircons. Foster et al. (2015) argued that the Neoarchean zircons were derived from the Congo and Kalahari Cratons, based on which we infer that Neoarchean zircons in the Zambezi Belt and the Damara Belt have similar sources. The Paleoproterozoic detrital zircons in southwestern Madagascar and the Damara Belt (ca. 2050–1700 Ma and 2150–1700 Ma, respectively, Collins et al., 2012; Boger et al., 2014; Foster et al., 2015) are comparable with ca. 2200–1700 Ma zircons from the Zambezi Belt. Collins et al. (2012) argued that the Usagaran Belt in Tanzania (2300–1800 Ma) could be a source of the late Paleoproterozoic detrital zircons in Madagascar. Although the Usagaran Belt might be a source of late Proterozoic detrital zircons in the Zambezi Belt, we regard the Magondi Belt in Zimbabwe (2000–1930 Ma, Munyanyiwa et al., 1995; Majaule et al., 2001; McCourt et al., 2001) could be a proximal source of the zircons. The late Mesoproterozoic detrital zircons in the Zambezi Belt show similar age population (ca. 1100 Ma) with those of the Mozambique and Damara Belts (ca. 1100 and 1050 Ma, respectively). Those from the Mozambique Belt could have been derived from the Nampula Complex (ca. 1150–1000 Ma, 950–700 Ma, Thomas et al., 2010), which we also regard as a source of the late Mesoproterozoic zircons in the Zambezi Belt. The middle Neoproterozoic detrital zircons (ca. 750 Ma) in the Zambezi Belt are likely to be comparable with those of southwestern Madagascar (ca. 800–700 Ma).

The age correlation summarized above indicates that the Zambezi Belt and the Damara Belt show similar age population of Neoproterozoic (ca. 2600–2700 Ma), Paleoproterozoic (ca. 2200–1700 Ma), and Mesoproterozoic to early Neoproterozoic (ca. 1500–900 Ma) (see Fig. 14). Foster et al. (2015) argued that the Archean to late Mesoproterozoic detrital zircons of the Damara Belt were derived from the Kalahari Craton. The detrital zircon ages of the Mozambique Belt is also similar to the age pattern of the Zambezi Belt, although late Paleoproterozoic to early Mesoproterozoic zircons (ca. 1800–1400 Ma) are absent in the Mozambique Belt. On the other hand, the Neoproterozoic to Paleoproterozoic ages of the detrital zircons of southwest Madagascar (ca. 2450–1550 Ma, 800–700 Ma) are comparable with those of the Zambezi Belt, whereas Mesoproterozoic zircons are absent in southwest Madagascar. We therefore conclude that metasediments of the Zambezi Belt and the Damara Belt might have similar sources.

5.4. Tectonic implications

Summarizing the discussion above, we present below a tectonic scenario around the Zambezi Belt (Fig. 15).

(1) Geochemistry data of orthogneisses suggest intracontinental rift-related magmatism during Neoarchean (ca. 2650 Ma) and

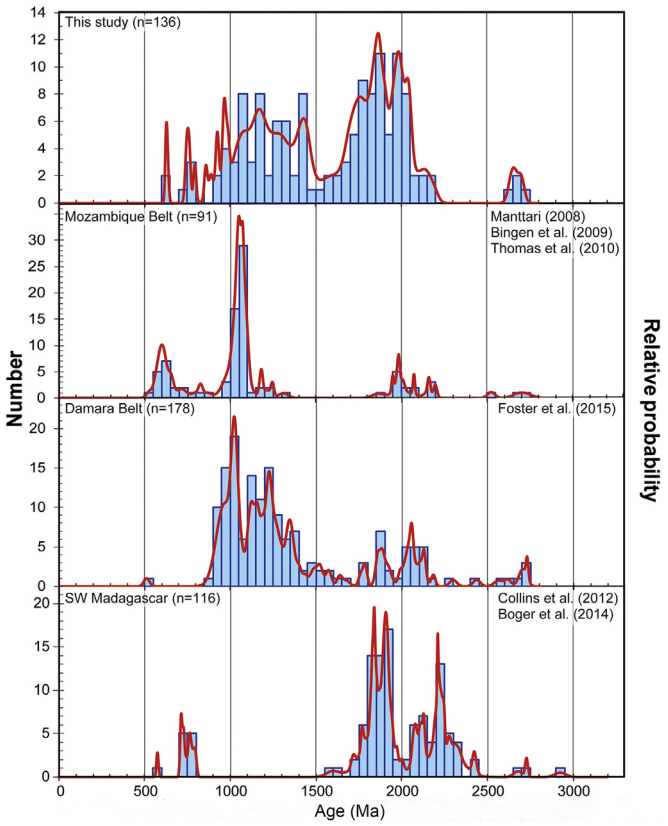

Figure 14. Histograms with probability density plots versus age (in Ma) of detrital zircon cores in the metasedimentary rocks from the Zambezi Belt, Mozambique Belt, Damara Belt, and southwestern Madagascar. Concordant (<10% discordance) detrital zircon ages were used to calculate the probability density plots. Older (>1.0 Ga) and younger (<1.0 Ga) ages are treated as $^{207}Pb/^{206}Pb$ and $^{206}Pb/^{238}U$ ages, respectively, therefore some published papers that discuss only $^{207}Pb/^{206}Pb$ and $^{206}Pb/^{238}U$ ages are not argued here. Data sources: Mozambique Belt (Mänttäri, 2008; Bingen et al., 2009; Thomas et al., 2010), Damara Belt (Foster et al., 2015), southwestern Madagascar (Collins et al., 2012; Boger et al., 2014).

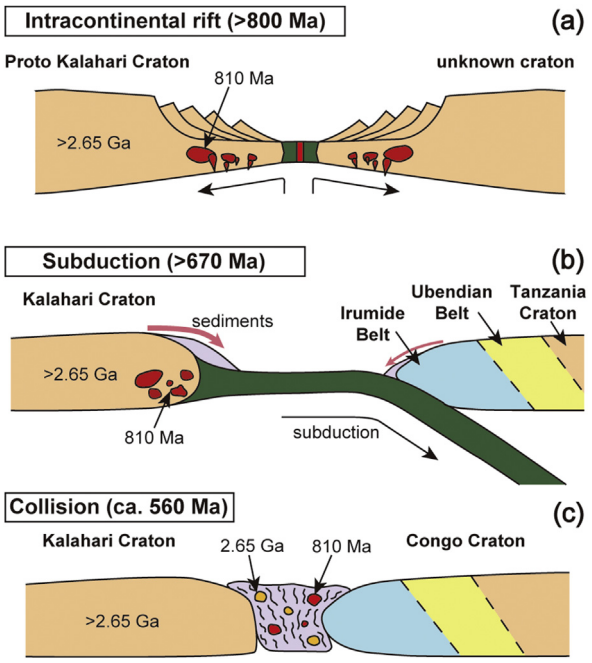

Figure 15. A schematic tectonic model illustrating geological history around the Zambezi Belt.

Early Neoproterozoic (ca. 880–740 Ma), although their detailed tectonic settings are not known. The Neoproterozoic event possibly associated with the break-up of Rodinia Supercontinent might have formed passive continental margins and an ocean basin between the Kalahari Craton and an unknown craton (Fig. 15a).

(2) Subduction of an oceanic plate beneath the southern margin of the Congo Craton that is composed of several crustal units such as Neoarchean craton (e.g., Tanzania Craton), Paleoproterozoic terrenes (e.g., Ubendian-Usagaran and Magondi Belts), and Mesoproterozoic terranes (e.g., Irumide Belt and Nampula Complexes) started before 670 Ma (Fig. 15b). Sediments with Neoarchean and Proterozoic detrital zircons reported in this study were possibly supplied from the two continents.

(3) During latest Neoproterozoic to early Cambrian (555–557 Ma), the final collision of the Kalahari and Congo Cratons related to the Kuunga Orogen occurred and formed a suture zone (Zambezi Belt) that contain fragments of ca. 2.65 Ga magmatic-arc units and ca. 800 Ma within-plate magmatic units (Fig. 15c). The high-grade metamorphism of the Zambezi Belt was caused by this collisional event.

6. Conclusions

(1) Metamorphic *P-T* conditions obtained for felsic orthogneisses from the western and central parts of the Marginal Gneiss Terrain are 700–780 °C/6.7–7.2 kbar and 680–800 °C/8.8–9.5 kbar, respectively. The *P-T* condition of meta-ultramafic rock and mafic orthogneiss from the Allochthonous Terrain are 650–690 °C/9.8–10.1 kbar and 800–875 °C/10–11 kbar, respectively. Such *P-T* variation suggests the Zambezi Belt correspond to a suture zone, and it may contain several crustal blocks with different *P-T* evolution.

(2) Geochemical and zircon U-Pb geochronological data of felsic orthogneisses indicate Neoarchean (2655 ± 21 Ma) and early Neoproterozoic (813 ± 5 Ma) within-plate magmatism under continental rift setting. The oldest zircon (2887 ± 13 Ma) is regarded as a xenocryst trapped during the intrusion of 2655 Ma felsic magma, suggesting reworking of Mesoarchean continental crust through Neoarchean thermal events.

(3) Detrital zircon cores from metasediments show four major age populations: Neoarchean (ca. 2700–2630 Ma), Paleoproterozoic (ca. 2200–1700 Ma), Mesoproterozoic (ca. 1500–950 Ma), and early Neoproterozoic (ca. 900–750 Ma). Most of them could have been derived from adjacent terranes such as the Kalahari Craton and the Lufilian Belt. The depositional age of the protolith sediments was constrained as 744–670 Ma.

(4) High-grade metamorphism possibly related to the collision of the Congo and Kalahari Cratons took place at 557–555 Ma, which is comparable with the available age of the Kuunga Orogen. Slightly older metamorphic age of 670–627 Ma from metasediments might be related to Cryogenian thermal events before the final collision.

Acknowledgement

We thank University of Zimbabwe (Department of Geology) and the Geological Survey of Zimbabwe for their support of geological fieldwork in 1999. We also thank National Museum of Nature and Science for analytical facilities and support. We thank two anonymous reviewers for their constructive review comments, and Guest Editor Prof. Alan Collins for his editorial comments and suggestions.

This study was partly supported by a Grant-in-Aid for Scientific Research (B) from Japan Society for the Promotion of Science (JSPS) (Nos. 26302009 and 18H01300) and by the NIPR General Collaboration Projects (No. 26-34) to Tsunogae.

Appendix A. Supplementary data

Supplementary data related to this article can be found at https://doi.org/10.1016/j.gsf.2018.05.019.

References

Armstrong, R.A., Master, S., Robb, L.J., 2005. Geochronology of the Nchanga granite, and constraints on the maximum age of the katanga supergroup, zambian copperbelt. Journal of African Earth Sciences 42, 32–40.

Arndt, N.T., Todt, W., Chauvel, C., Tapfer, M., Weber, K., 1991. U-Pb zircon age and Nd isotopic composition of granitoids, charnockites and supracrustal rocks from Heimefrontfjella, Antarctica. Geologische Rundschau 80, 759–777.

Bache, J.J., Dallas, S., Prost, A.E., 1982. A preliminary report on the geology of the country north of Mount Darwin. Annals of the Zimbabwe Geological Survey VIII, 30–35.

Barton, C.M., Carney, J.N., Crow, M.J., Dunkley, P.N., Simango, S., 1991. The geology of the country around Rushinga and Nyamapanda. Zimbabwe Geological Survey Bulletin 92.

Barton, C.M., Carney, J.N., Evans, J.A., Simango, S., 1993. Geological and structural framework of the Zambezi belt, northeastern Zimbabwe. In: Findlay, R.H., Unrug, R., Banks, M.R., Veevers, J.J. (Eds.), Gondwana Eight. Balkema, Rotterdam, pp. 55–68.

Batumike, J.M., Griffin, W.L., O'Reilly, S.Y., Belousova, E.A., Pawlitschek, M., 2009. Crustal evolution in the central Congo-Kasai Craton, Luebo, DR Congo: insights from zircon U–Pb ages, Hf-isotope and trace-element data. Precambrian Research 170, 107–115.

Bingen, B., Jacobs, J., Viola, G., Henderson, I.H.C., Skår, Ø., Boyd, R., Thomas, R.J., Solli, A., Key, R.M., Daudi, E.X.F., 2009. Geochronology of the Precambrian crust in the Mozambique belt in NE Mozambique, and implications for Gondwana assembly. Precambrian Research 170, 231–255.

Bisnath, A., Frimmel, H.E., Armstrong, R.A., Board, W.S., 2006. Tectono-thermal evolution of the Maud belt: new SHRIMP U–Pb zircon data from gjelsvikfjella, dronning Maud land, east Antarctica. Precambrian Research 150, 95–121.

Board, W.S., Frimmel, H.E., Armstrong, R.A., 2004. Pan-African tectonism in the western Maud Belt: P–T–t path for high-grade gneisses in the HU Sverdrupfjella, East Antarctica. Journal of Petrology 46, 671–699.

Boger, S.D., Hirdes, W., Ferreira, C.A.M., Schulte, B., Jenett, T., Fanning, C.M., 2014. From passive margin to volcano–sedimentary forearc: the Tonian to Cryogenian evolution of the Anosyen Domain of southeastern Madagascar. Precambrian Research 247, 159–186.

Bulambo, M., De Waele, B., Kampunzu, A.B., Tembo, F., 2004. SHRIMP U-Pb geochronology of the Choma-Kalomo block (Zambia) and geological implications. In: Abstracts Volume, 20th Colloquium of African Geology, Orléans, France.

Bulambo, M., De Waele, B., Kokonyangi, J., Johnson, S.P., Kampunzu, A.B., Tembo, F., 2006. SHRIMP zircon U-Pb geochronology and geochemistry of the Choma-Kalomo Block granitoids (Zambia): geological implications. In: Abstracts Volume, 21st Colloquium of African Geology, Maputo, Mozambique.

Burger, A.J., Clifford, T.N., Miller, R.M., 1976. Zircon U-Pb ages of the franzfontein granitic suite, northern south west Africa. Precambrian Research 3, 415–431.

Cabanis, B., Lecolle, M., 1989. Le diagramme La/10-Y/15-Nb/8: un outil pour la discrimination des series volcaniques et la mise en evidence des processus demelange et/ou de contamination crustale. Comptes Rendus de l'Académie des Sciences Serie 2 (309), 2023–2029 (in French).

Caen-Vachette, M., Vialette, Y., Bassot, J.P., Vidal, P., 1988. Apport de la géochronologie isotopique à la connaissance de la géologie Gabonaise. Chronique de la Recherche Miniere 491, 35–54 (in French).

Cahen, L., Snelling, N.J., Delhal, J., Vail, J.R., 1984. The Geochronology and Evolution of Africa. Clarendon Press, Oxford, p. 512 pp.

Carney, J.N., Treloar, P.J., Barton, C.M., Crow, M.J., Evans, J.A., Simango, S., 1991. Deep-crustal granulites with migmatitic and mylonitic fabrics from the Zambezi belt, northeastern Zimbabwe. Journal of Metamorphic Geology 9, 461–479.

Collins, A.S., Pisarevsky, S.A., 2005. Amalgamating eastern Gondwana: the evolution of the circum-indian orogens. Earth-Science Reviews 71, 229–270.

Collins, A.S., Windley, B.F., 2002. The tectonic evolution of central and northern Madagascar and its place in the final assembly of Gondwana. The Journal of Geology 110, 325–339.

Collins, A.S., Reddy, S.M., Buchan, C., Mruma, A., 2004. Temporal constraints on Palaeoproterozoic eclogite formation and exhumation (Usagaran Orogen, Tanzania). Earth and Planetary Science Letters 224, 175–192.

Collins, A.S., Clark, C., Sajeev, K., Santosh, M., Kelsey, D.E., Hand, M., 2007a. Passage through India: the Mozambique ocean suture, high pressure granulites and the palghat-cauvery shear system. Terra Nova 19, 141–147.

Collins, A.S., Santosh, M., Braun, I., Clark, C., 2007b. Age and sedimentary provenance of the Southern Granulites, South India: U–Th–Pb SHRIMP secondary ion mass spectrometry. Precambrian Research 155, 125–138.

Collins, A.S., Kinny, P.D., Razakamanana, T., 2012. Depositional age, provenance and metamorphic age of metasedimentary rocks from southern Madagascar. Gondwana Research 21, 353–361.

Corfu, F., Hanchar, J.M., Hoskin, P.W.O., Kinny, P., 2003. Atlas of zircon textures. Reviews in Mineralogy and Geochemistry 53, 469–500.

Costa, M., Cadoppi, P., Sacchi, R., Fanning, C.M., 1994. U-Pb" SHRIMP" dating of zircons from Mozambique gneiss. Bollettino Della Societa Geologica Italiana 113, 173–178.

Coward, M.P., Daly, M.C., 1984. Crustal Lineaments and shear zones in Africa: their relationship to plate movements. Precambrian Research 24, 27–45.

de Kock, M.O., Ernst, R., Söderlund, U., Jourdan, F., Hofmann, A., Gall, B.L., Bertrand, H., Chisonga, B.C., Beukes, N., Rajesh, H.M., Moseki, L.M., Fuchs, R., 2014. Dykes of the 1.11 Ga Umkondo LIP, southern Africa: clues to a complex plumbing system. Precambrian Research 249, 129–143.

De Waele, B., Nemchin, A.A., Kampunzu, A.B., 2003a. The Bangweulu Block of northern Zambia: where is the preUbendian crust?. In: Assembly and Breakup of Rodinia, IGCP 440 South China Field Symposium, Hangzhou, China, pp. 19–21.

De Waele, B., Wingate, M.T.D., Fitzsimons, I.C.W., Mapani, B.S.E., 2003b. Untying the Kibaran knot: a reassessment of Mesoproterozoic correlations in southern Africa based on SHRIMP U-Pb data from the Irumide belt. Geology 31, 509–512.

De Waele, B., Liégeois, J.P., Nemchin, A.A., Tembo, F., 2006a. Isotopic and geochemical evidence of Proterozoic episodic crustal reworking within the Irumide Belt of south-central Africa, the southern metacratonic boundary of an Archaean Bangweulu Craton. Precambrian Research 148, 225–256.

De Waele, B., Kampunzu, A.B., Mapani, B.S.E., Tembo, F., 2006b. The mesoproterozoic Irumide belt of Zambia. Journal of African Earth Sciences 46, 36–70.

Deblond, A., Punzalan, L.E., Boven, A., Tack, L., 2001. The Malagarazi Supergroup of southeast Burundi and its correlative Bukoba Supergroup of northwest Tanzania: neo- and Mesoproterozoic chronostratigraphic constraints from Ar-Ar ages on mafic intrusive rocks. Journal of African Earth Sciences 32, 435–449.

Delhal, J., Ledent, D., Torquato, J., 1976. Nouvelles données géochronologiques relatives au complexe gabbro-noritique et charnockitique du bouclier du Kasai et son prolongement en Angola. Annales de la Société Géologique de Belgique 99, 211–226 (in French).

Dirks, P.H., Jelsma, H.A., 2006. The structural-metamorphic evolution of the northern margin of the Zimbabwe craton and the adjacent Zambezi belt in northeastern Zimbabwe. Geological Society of America Special Papers 405, 291–313.

Dirks, P.H.G.M., Jelsma, H.A., Vinyu, M., Munyanyiwa, H., 1998. The structural history of the Zambezi belt in northeast Zimbabwe; evidence for crustal extension during the early Pan-African. South African Journal of Geology 101, 1–16.

Dirks, P.H.G.M., Kröner, A., Jelsma, H.A., Sithole, T.A., Vinyu, M.L., 1999. Structural relations and Pb–Pb zircon ages for the Makuti gneisses: evidence for a crustal-scale Pan-African shear zone in the Zambezi belt, northwest Zimbabwe. Journal of African Earth Sciences 28, 427–442.

Dunkley, D.J., Shiraishi, K., Motoyoshi, Y., Tsunogae, T., Miyamoto, T., Hiroi, Y., Carson, C.J., 2014. Deconstructing the lützow–holm complex with zircon geochronology. In: Abstract of 7th International SHRIMP Workshop Program, pp. 116–121.

Eggins, S.M., Kinsley, L.P.J., Shelley, J.M.G., 1998. Deposition and element fractionation processes during atmospheric pressure laser sampling for analysis by ICP-MS. Applied Surface Science 127–129, 278–286.

Endo, T., Tsunogae, T., Santosh, M., Shaji, E., Rambeloson, R.A., 2017. Petrogenesis of incipient charnockite in the Ikalamavony sub-domain, south-central Madagascar: new insights from phase equilibrium modeling. Lithos 282–283, 431–446.

Foley, S.F., Barth, M.G., Jenner, G.A., 2000. Rutile/melt partition coefficients for trace elements and an assessment of the influence of rutile on the trace element characteristics of subduction zone magmas. Geochimica et Cosmochimica Acta 64, 933–938.

Foster, D.A., Goscombe, B.D., Newstead, B., Mapani, B., Mueller, P.A., Gregory, L.C., Muvangua, E., 2015. U–Pb age and Lu–Hf isotopic data of detrital zircons from the neoproterozoic Damara sequence: implications for Congo and Kalahari before Gondwana. Gondwana Research 28, 179–190.

Franz, L., Romer, R.L., Dingeldey, D.P., 1999. Diachronous Pan-African granulite-facies metamorphism (650 Ma and 550 Ma) in the kaoko belt, NW Namibia. European Journal of Mineralogy 11, 167–180.

Glynn, S., Wiedenbeck, M., Master, S., Frei, D., 2015. New U-Pb zircon geochronology of the choma-kalomo block (Zambia) and the dete-kamativi inlier (Zimbabwe), with implications for the extent of the Zimbabwe craton. In: Abstracts Volume, European Geosciences Union General Assembly, Vienna, Austria.

Goscombe, B., Armstrong, R., Barton, J.M., 2000. Geology of the Chewore Inliers, Zimbabwe: constraining the mesoproterozoic to palaeozoic evolution of the Zambezi belt. Journal of African Earth Sciences 30, 589–627.

Graham, C.M., Powell, R., 1984. A garnet–hornblende geothermometer: calibration, testing, and application to the Pelona Schist, Southern California. Journal of Metamorphic Geology 2, 13–31.

Grantham, G.H., Macey, P.H., Ingram, B.A., Roberts, M.P., Armstrong, R.A., Hokada, T., Shiraishi, K., Jackson, C., Bisnath, A., Manhica, V., 2008. Terrane correlation between Antarctica, Mozambique and Sri Lanka; comparisons of

geochronology, lithology, structure and metamorphism and possible implications for the geology of southern Africa and Antarctica. Geological Society, London, Special Publications 308, 91–119.
Green, E.C.R., White, R.W., Diener, J.F.A., Powell, R., Holland, T.J.B., Palin, R.M., 2016. Activity–composition relations for the calculation of partial melting equilibria in metabasic rocks. Journal of Metamorphic Geology 34, 845–869.
Hammarstrom, J.M., Zen, E.A., 1986. Aluminum in hornblende: an empirical igneous geobarometer. American Mineralogist 71, 1297–1313.
Hanson, R.E., 2003. Proterozoic geochronology and tectonic evolution of southern Africa. Geological Society, London, Special Publications 206, 427–463.
Hanson, R.E., Wilson, T.J., Brueckner, H.K., Onstott, T.C., Wardlaw, M.S., Johns, C.C., Hardcastle, K.C., 1988a. Reconnaissance geochronology, tectonothermal evolution, and regional significance of the Middle Proterozoic Choma-Kalomo block, southern Zambia. Precambrian Research 42, 39–61.
Hanson, R.E., Wilson, T.J., Wardlaw, M.S., 1988b. Deformed batholiths in the Pan-African Zambezi belt, Zambia: age and implications for regional Proterozoic tectonics. Geology 16, 1134–1137.
Hanson, R.E., Hargrove, U.S., Martin, M.W., Bowring, S.A., Krol, M.A., Hodges, K.V., Munyanyiwa, H., Blenkinsop, T.G., 1998. New geochronological constraints on the tectonic evolution of the Pan-African Zambezi belt, south-central Africa. Journal of African Earth Sciences 27, 104–105 (special abstracts issue, 10th International Gondwana Conference).
Hargrove, U.S., Hanson, R.E., Martin, M.W., Blenkinsop, T.G., Bowring, S.A., Walker, N., Munyanyiwa, H., 2003. Tectonic evolution of the Zambezi orogenic belt: geochronological, structural, and petrological constraints from northern Zimbabwe. Precambrian Research 123, 159–186.
He, X.F., Santosh, M., Zhang, Z.M., Tsunogae, T., Chetty, T.R.K., Ram Mohan, M., Anbazhagan, S., 2015. Shonkinites from Salem, southern India: implications for Cryogenian alkaline magmatism in rift-related setting. Journal of Asian Earth Sciences 113, 812–825.
He, X.F., Santosh, M., Tsunogae, T., Malaviarachchi, S.P.K., 2016a. Early to late Neoproterozoic magmatism and magma mixing–mingling in Sri Lanka: implications for convergent margin processes during Gondwana assembly. Gondwana Research 32, 151–180.
He, X.F., Santosh, M., Tsunogae, T., Malaviarachchi, S.P.K., Dharmapriya, P.L., 2016b. Neoproterozoic arc accretion along the 'eastern suture' in Sri Lanka during Gondwana assembly. Precambrian Research 279, 57–80.
Holland, T., Blundy, J., 1994. Non-ideal interactions in calcic amphiboles and their bearing on amphibole-plagioclase thermometry. Contributions to Mineralogy and Petrology 116, 433–447.
Holland, T.J.B., Powell, R., 1998. An enlarged and update internally consistent thermodynamic dataset with uncertainties and correlations: the system K_2O–Na_2O–CaO–MgO–MnO–FeO–Fe_2O_3–Al_2O_3–TiO_2–SiO_2–C–H_2–O_2. Journal of Metamorphic Geology 8, 89–124.
Holland, T.J.B., Powell, R., 2003. Activity–composition relations for phases in petrological calculations: an asymmetric multicomponent formulation. Contributions to Mineralogy and Petrology 145, 492–501.
Holland, T.J.B., Powell, R., 2011. An improved and extended internally consistent thermodynamic dataset for phases of petrological interest, involving a new equation of state for solids. Journal of Metamorphic Geology 29, 333–383.
Ishii, S., Tsunogae, T., Santosh, M., 2006. Ultrahigh-temperature metamorphism in the Achankovil Zone: implications for the correlation of crustal blocks in southern India. Gondwana Research 10, 99–114.
Jacobs, J., Thomas, R.J., 2004. Himalayan-type indenter-escape tectonics model for the southern part of the late Neoproterozoic-early Paleozoic East African-Antarctic orogen. Geology 32, 721–724.
Jacobs, J., Fanning, C.M., Henjes-Kunst, F., Olesch, M., Paech, H.J., 1998. Continuation of the Mozambique belt into east Antarctica: grenville-age metamorphism and polyphase Pan-African high-grade events in central dronning Maud land. The Journal of Geology 106, 385–406.
Jacobs, J., Bauer, W., Fanning, C.M., 2003. Late neoproterozoic/early palaeozoic events in central dronning Maud land and significance for the southern extension of the east african orogen into east Antarctica. Precambrian Research 126, 27–53.
John, T., Schenk, V., Haase, K., Scherer, E., Tembo, F., 2003. Evidence for a Neoproterozoic ocean in south-central Africa from mid-oceanic-ridge–type geochemical signatures and pressure-temperature estimates of Zambian eclogites. Geology 31, 243–246.
John, T., Schenk, V., Mezger, K., Tembo, F., 2004. Timing and PT evolution of whiteschist metamorphism in the Lufilian Arc–Zambezi Belt orogen (Zambia): implications for the assembly of Gondwana. The Journal of Geology 112, 71–90.
Johnson, S.P., De Waele, B., Liyungu, K.A., 2006. U-Pb sensitive high-resolution ion microprobe (SHRIMP) zircon geochronology of granitoid rocks in eastern Zambia: terrane subdivision of the Mesoproterozoic Southern Irumide Belt. Tectonics 25, TC6004,. https://doi.org/10.1029/2006TC001977.
Johnson, S.P., De Waele, B., Evans, D., Banda, W., Tembo, F., Milton, J.A., Tani, K., 2007. Geochronology of the Zambezi supracrustal sequence, southern Zambia: a record of Neoproterozoic divergent processes along the southern margin of the Congo Craton. The Journal of Geology 115, 355–374.
Kabete, J.M., McNaughton, N.J., Groves, D.I., Mruma, A.H., 2012. Reconnaissance SHRIMP U–Pb zircon geochronology of the Tanzania craton: evidence for neoarchean granitoid–greenstone belts in the Central Tanzania region and the southern east african orogen. Precambrian Research 216–219, 232–266.
Kampunzu, A.B., Armstrong, R., Modisi, M.P., Mapeo, R.B., 2000. Ion microprobe U-Pb ages on detrital zircon grains from the Ghanzi Group: implications for the identification of a Kibaran-age crust in northwest Botswana. Journal of African Earth Sciences 30, 579–587.
Katongo, C., Koller, F., Kloetzli, U., Koeberl, C., Tembo, F., De Waele, B., 2004. Petrography, geochemistry and geochronology of granitoid rocks in the Neoproterozoic–Paleozoic Lufilian-Zambezi belt, Zambia: implications for tectonic setting and regional correlation. Journal of African Earth Sciences 40, 219–244.
Kawakami, T., Hokada, T., Sakata, S., Hirata, T., 2016. Possible polymetamorphism and brine infiltration recorded in the garnet–sillimanite gneiss, Skallevikshalsen, Lützow–Holm Complex, East Antarctica. Journal of Mineralogical and Petrological Sciences 111, 129–143.
Kazami, S., Tsunogae, T., Santosh, M., Tsutsumi, Y., Takamura, Y., 2016. Petrology, geochemistry and zircon U–Pb geochronology of a layered igneous complex from Akarui Point in the Lützow–Holm Complex, East Antarctica: implications for Antarctica–Sri Lanka correlation. Journal of Asian Earth Sciences 130, 206–222.
Key, R.M., Liyungu, A.K., Njamu, F.M., Somwe, V., Banda, J., Mosley, P.N., Armstrong, R.A., 2001. The western arm of the Lufilian Arc in NW Zambia and its potential for copper mineralization. Journal of African Earth Sciences 33, 503–528.
Kinny, P.D., Wijbrans, J.R., Froude, D.O., Williams, I.S., Compston, W., 1990. Age constraints on the geological evolution of the narryer gneiss complex, western Australia. Australian Journal of Earth Sciences 37, 51–69.
Kohn, M.J., Spear, F.S., 1990. Two new geobarometers for garnet amphibolites, with applications to southeastern Vermont. American Mineralogist 75, 89–96.
Koizumi, T., Tsunogae, T., Santosh, M., Tsutsumi, Y., Chetty, T.R.K., Saitoh, Y., 2014. Petrology and zircon U-Pb geochronology of metagabbros from a mafic-ultramafic suite at Aniyapuram: Neoarchean to Early Paleoproterozoic convergent margin magmatism and Neoproterozoic high-grade metamorphism in southern India. Journal of Asian Earth Sciences 95, 51–64.
Kokonyangi, J., Armstrong, R., Kampunzu, A.B., Yoshida, M., Okudaira, T., 2004. U–Pb zircon geochronology and petrology of granitoids from Mitwaba (Katanga, Congo): implications for the evolution of the Mesoproterozoic Kibaran belt. Precambrian Research 132, 79–106.
Kröner, A., Sacchi, R., Jaeckel, P., Costa, M., 1997. Kibaran magmatism and Pan-African granulite metamorphism in northern Mozambique: single zircon ages and regional implications. Journal of African Earth Sciences 25, 467–484.
Leake, B.E., Woolley, A.R., Arps, C.E.S., Birch, W.D., Gilbert, M.C., Grice, J.D., Hawthorne, F.C., Kato, A., Kisch, H.J., Krivovichev, V.G., Linthout, K., Laird, J., Mandarino, J.A., Maresch, W.V., Nickel, E.H., Rock, N.M.S., Schumacher, J.C., Smith, D.C., Stephenson, N.C.N., Ungaretti, L., Whittaker, E.J.W., Youzhi, G., 1997. Nomenclature of amphiboles: report of the subcommittee on amphiboles of the International Mineralogical Association, commission on new minerals and mineral names. American Mineralogist 82, 1019–1037.
Leitner, E.G., Phaup, A.E., 1974. The geology of the country around Mount Darwin. Rhodesia Geological Survey Bulletin 73, 151 pp.
Lenoir, J.L., Liégeois, J.P., Theunissen, K., Klerkx, J., 1994. The Palaeoproterozoic Ubendian shear belt in Tanzania: geochronology and structure. Journal of African Earth Sciences 19, 169–184.
Ludwig, K.R., 2008. User's Manual for Isoplot 3.70. Berkeley Geochronology Center Special Publication, No. 4, p. 70.
Luft Jr., J.L., Chemale Jr., F., de Fátima Bitencourt, M., 2001. Significance of Paleoproterozoic to Neoproterozoic ages in the Kaoko Belt, NW Namibia. Gondwana Research 4, 693.
Maas, R., Kinny, P.D., Williams, I.S., Froude, D.O., Compston, W., 1992. The Earth's oldest known crust: a geochronological and geochemical study of 3900–4200 Ma old detrital zircons from Mt. Narryer and Jack Hills, Western Australia. Geochimica et Cosmochimica Acta 56, 1281–1300.
Majaule, T., Hanson, R.E., Key, R.M., Singletary, S.J., Martin, M.W., Bowring, S.A., 2001. The Magondi Belt in northeast Botswana: regional relations and new geochronological data from the Sua Pan area. Journal of African Earth Sciences 32, 257–267.
Mänttäri, I., 2008. Mesoarchaean to Lower Jurassic U-Pb and Sm-Nd ages from NW Mozambique. Geological Survey of Finland Special paper 48, 81–119.
Mariga, J., 1999. Structural and Geochronological Evolution of Deep-crustal Granulites, Supracrustal Rocks, and Deformed Plutons in the Zambezi Orogenic Belt, Rusambo Mission Area, Northeastern Zimbabwe. M.S. thesis. Texas Christian University, p. 110 pp.
Mariga, J., Hanson, R.E., Martin, M.W., Singletary, S.J., Bowring, S.A., 1998. Timing of polyphase ductile deformation at deep to mid-crustal levels in the Neoproterozoic Zambezi belt, NE Zimbabwe. Geological Society of America Abstracts with Programs 30, A292.
Master, S., Glynn, S.M., Wiedenbeck, M., 2015. The vanished orogeny: Geochronology of Palaeoproterozoic "basement" gneisses of the Kariba and adjacent areas, western Magondi Belt (Zimbabwe and Zambia). In: Abstracts Volume, Geological Society of Zimbabwe Annual Summer Symposium, Kariba, Zimbabwe.
McCourt, S., Hilliard, P., Armstrong, R.A., Munyanyiwa, H., 2001. SHRIMP U-Pb zircon geochronology of the Hurungwe granite northwest Zimbabwe: Age constraints on the timing of the Magondi orogeny and implications for the correlation between the Kheis and Magondi Belts. South African Journal of Geology 104, 39–46.
McDonough, W.F., Sun, S.-S., 1995. The composition of the Earth. Chemical Geology 120, 223–253.

Meert, J., 2003. A synopsis of events related to the assembly of eastern Gondwana. Tectonophysics 362, 1–40.
Meert, J.G., Lieberman, B.S., 2008. The Neoproterozoic assembly of Gondwana and its relationship to the Ediacaran-Cambrian radiation. Gondwana Research 14, 5–21.
Meert, J.G., Voo, R.V.D., 1997. The assembly of Gondwana 800–550 Ma. Journal of Geodynamics 23, 223–235.
Meert, J., Voo, R.V.D., Ayub, S., 1995. Paleomagnetic investigation of the Neoproterozoic Gagwe lavas and Mbozi complex, Tanzania and the assembly of Gondwana. Precambrian Research 74, 225–244.
Meschede, M., 1986. A method of discriminating between different types of mid-ocean ridge basalts and continental tholeiites with the Nb–Zr–Y diagram. Chemical Geology 56, 207–218.
Mullen, E.D., 1983. $MnO/TiO_2/P_2O_5$ a minor element discriminations for basaltic rocks of oceanic environments and its implications for petrogenesis. Earth and Planetary Science Letters 62, 53–62.
Müller, M., 2004. The Mavuradonha Layered Complex: Neoproterozoic Emplacement and Pan-African Granulite-facies Metamorphism in the Zambezi Allochthonous Terrane of the Mt. Darwin Area, Zambezi Belt, NE-Zimbabwe. Darwin Area, Zambezi Belt, NE-Zimbabwe. Ph. D. thesis. Johannes Gutenberg University, p. 266 pp.
Munyanyiwa, H., Kröner, A., Jaeckel, P., 1995. U-Pb and Pb-Pb single zircon ages for charno-enderbites from the Magondi mobile belt, northwest Zimbabwe. South African Journal of Geology 98, 52–57.
Munyanyiwa, H., Hanson, R.E., Blenkinsop, T.G., Treloar, P.J., 1997. Geochemistry of amphibolites and quartzofeldspathic gneisses in the Pan-African Zambezi belt, NW Zimbabwe: evidence for bimodal magmatism in a continental rift setting. Precambrian Research 81, 179–196.
Nelson, D.R., 2001. An assessment of the determination of depositional ages for Precambrian clastic sedimentary rocks by U-Pb dating of detrital zircons. Sedimentary Geology 141–142, 37–60.
Paces, J.B., Miller, J.D., 1993. Precise U–Pb ages of Duluth Complex and related mafic intrusions, northeastern Minnesota: geochronological insights to physical, petrogenetic, paleomagnetic and tectonomagmatic processes associated with the 1.1 Ga midcontinent rift system. Journal of Geophysical Research 98, 13997–14013.
Paulsson, O., Austrheim, H., 2003. A geochronological and geochemical study of rocks from Gjelsvikfjella, Dronning Maud Land, Antarctica—implications for Mesoproterozoic correlations and assembly of Gondwana. Precambrian Research 125, 113–138.
Pearce, J.A., 2008. Geochemical fingerprinting of oceanic basalts with applications to ophiolite classification and the search for Archean oceanic crust. Lithos 100, 14–48.
Pearce, J.A., Harris, N.B.W., Tindle, A.G., 1984. Trace element discrimination diagrams for the tectonic interpretation of granitic rocks. Journal of Petrology 25, 956–983.
Porada, H., Berhorst, V., 2000. Towards a new understanding of the Neoproterozoic–Early Palaeozoic Lufilian and Zambezi belts in Zambia and the Democratic Republic of Congo. Journal of African Earth Sciences 30, 717–771.
Powell, R., Holland, T.J.B., 1988. An internally consistent thermodynamic dataset with uncertainties and correlations: 3. Application, methods, worked examples and a computer program. Journal of Metamorphic Geology 6, 173–204.
Priem, H.N.A., Boelrijk, N.A.I.M., Hebeda, E.H., Verdurmen, E.A.T., Verschure, R.H., 1971. Isotopic dating in the Kamativi Tin Belt, southern Rhodesia. Geologie en Mijinbouw 50, 619–624.
Ravna, E.K., 2000. Distribution of Fe^{2+} and Mg between coexisting garnet and hornblende in synthetic and natural systems: an empirical calibration of the garnet–hornblende Fe–Mg geothermometer. Lithos 53, 265–277.
Ring, U., Kröner, A., Toulkeridis, T., 1997. Palaeoproterozoic granulite-facies metamorphism and granitoid intrusions in the Ubendian-Usagaran Orogen of northern Malawi, east-central Africa. Precambrian Research 85, 27–51.
Sajeev, K., Osanai, Y., 2004. Ultrahigh-temperature metamorphism (1150 C, 12 kbar) and multistage evolution of Mg-, Al-rich granulites from the central Highland Complex, Sri Lanka. Journal of Petrology 45, 1821–1844.
Sanislav, I.V., Wormald, R.J., Dirks, P.H.G.M., Blenkinsop, T.G., Salamba, L., Joseph, D., 2014. Zircon U–Pb ages and Lu–Hf isotope systematics from late-tectonic granites, Geita Greenstone Belt: Implications for crustal growth of the Tanzania Craton. Precambrian Research 242, 187–204.
Santosh, M., Maruyama, S., Sato, K., 2009a. Anatomy of a Cambrian suture in Gondwana: Pacific-type orogeny in southern India? Gondwana Research 16, 321–341.
Santosh, M., Maruyama, S., Yamamoto, S., 2009b. The making and breaking of supercontinents: some speculations based on superplumes, superdownwelling and the role of tectosphere. Gondwana Research 15, 324–341.
Santosh, M., Xiao, W.J., Tsunogae, T., Chetty, T.R.K., Yellappa, T., 2012. The Neoproterozoic subduction complex in southern India: SIMS zircon U–Pb ages and implications for Gondwana assembly. Precambrian Research 192–195, 190–208.
Santosh, M., Shaji, E., Tsunogae, T., Ram Mohan, M., Satyanarayanan, M., Horie, K., 2013. Suprasubduction zone ophiolite from Agali hill: petrology, zircon SHRIMP U–Pb geochronology, geochemistry and implications for Neoarchean plate tectonics in southern India. Precambrian Research 231, 301–324.
Santosh, M., Tsunogae, T., Malaviarachchi, S.P.K., Zhang, Z., Ding, H., Tang, L., Dharmapriya, P.L., 2014. Neoproterozoic crustal evolution in Sri Lanka: insights from petrologic, geochemical and zircon U–Pb and Lu–Hf isotopic data and implications for Gondwana assembly. Precambrian Research 255, 1–29.
Santosh, M., Yang, Q.Y., Shaji, E., Ram Mohan, M., Tsunogae, T., Satyanarayanan, M., 2016. Oldest rocks from Peninsular India: evidence for Hadean to Neoarchean crustal evolution. Gondwana Research 29, 105–135.
Santosh, M., Hu, C.-N., He, X.-F., Li, S.-S., Tsunogae, T., Shaji, E., Indu, G., 2017. Neoproterozoic arc magmatism in the southern Madurai Block, India: Subduction, relamination, continental outbuilding, and the growth of Gondwana. Gondwana Research 45, 1–42.
Schmidt, M.W., 1992. Amphibole composition in tonalite as a function of pressure: an experimental calibration of the Al-in-hornblende barometer. Contributions to Mineralogy and Petrology 110, 304–310.
Schwartz, M.O.K., Kwok, Y.Y., Davis, D.W., Akanyang, P., 1996. Geology, geochronology and regional correlation of the Ghanzi Ridge, Botswana. South African Journal of Geology 99, 245–250.
Seth, B., Kröner, A., Mezger, K., Nemchin, A.A., Pidgeon, R.T., Okrusch, M., 1998. Archaean to Neoproterozoic magmatic events in the Kaoko belt of NW Namibia and their geodynamic significance. Precambrian Research 92, 341–363.
Shimizu, H., Tsunogae, T., Santosh, M., 2009. Spinel + quartz assemblage in granulites from the Achankovil Shear Zone, southern India: implications for ultrahigh-temperature metamorphism. Journal of Asian Earth Sciences 36, 209–222.
Singletary, S.J., Hanson, R.E., Martin, M.W., Crowley, J.L., Bowring, S.A., Key, R.M., Ramokate, L.C., Direng, B.B., Krol, M.A., 2003. Geochronology of basement rocks in the Kalahari Desert, Botswana, and implications for regional Proterozoic tectonics. Precambrian Research 121, 47–71.
Stacey, J.S., Kramers, J.D., 1975. Approximation of terrestrial lead isotope evolution by a two-stage model. Earth and Planetary Science Letters 26, 207–221.
Sun, S.-S., McDonough, W.F., 1989. Chemical and isotopic systematics of oceanic basalts: implications for mantle composition and processes. In: Saunders, A.D., Norry, M.J. (Eds.), Magmatism in the Ocean Basins. Geological Society, London, Special Publications 42, 313–345.
Tack, L., Fernandez-Alonso, M., Tahon, A., Wingate, M.T.D., 2002. Meso and Neoproterozoic emplacement ages of magmatic rocks in Burundi: new constraints for the geodynamic evolution of the Northeastern Kibaran belt (NKB). Abstract Volume IGCP 418, 440.
Takahashi, K., Tsunogae, T., Santosh, M., Takamura, Y., Tsutsumi, Y., 2018. Paleoproterozoic (ca. 1.8 Ga) arc magmatism in the Lützow-Holm Complex, East Antarctica: implications for crustal growth and terrane assembly in erstwhile Gondwana fragments. Journal of Asian Earth Sciences 157, 245–268.
Takamura, Y., Tsunogae, T., Santosh, M., Malaviarachchi, S.P.K., Tsutsumi, Y., 2015. Petrology and zircon U-Pb geochronology of metagabbro from the Highland Complex, Sri Lanka: Implications for the correlation of Gondwana suture zones. Journal of Asian Earth Sciences 113, 826–841.
Takamura, Y., Tsunogae, T., Santosh, M., Malaviarachchi, S.P.K., Tsutsumi, Y., 2016. U–Pb geochronology of detrital zircon in metasediments from Sri Lanka: implications for the regional correlation of Gondwana fragments. Precambrian Research 281, 434–452.
Takamura, Y., Tsunogae, T., Santosh, M., Tsutsumi, Y., 2018. Detrital zircon geochronology of the Lützow-Holm Complex, East Antarctica: Implications for Antarctica - Sri Lanka correlation. Geoscience Frontiers 9, 355–375.
Tchameni, R., Mezger, K., Nsifa, N.E., Pouclet, A., 2000. Neoarchean crustal evolution in the Congo Craton: evidence from K-rich granitoids of the Ntem Complex, southern Cameroon. Journal of African Earth Sciences 30, 133–147.
Tegtmeyer, A., Kröner, A., 1985. U-Pb zircon ages for granitoid gneisses in northern Namibia and their significance for Proterozoic crustal evolution of southwestern Africa. Precambrian Research 28, 311–326.
Thiéblemont, D., 1999. Discrimination entre magmatismes calco-alcalins mantellique et crustal: l'exemple des Andes. Comptes Rendus de l'Academie des Sciences - Series IIA: Earth and Planetary Science 329, 243–250.
Thiéblemont, D., Tegyey, M., 1994. Geochemical discrimination of differentiated magmatic rocks attesting for the variable origin and tectonic setting of calc-alkaline magmas. Comptes Rendus De L Academie Des Sciences Serie II 319, 87–94.
Thomas, R.J., Jacobs, J., Horstwood, M.S.A., Ueda, K., Bingen, B., Matola, R., 2010. The Mecubúri and Alto Benfica groups, NE Mozambique: Aids to unravelling ca. 1 and 0.5 Ga events in the east African orogen. Precambrian Research 178, 72–90.
Thomas, R.J., Roberts, N.M.W., Jacobs, J., Bushi, A.M., Horstwood, M.S.A., Mruma, A., 2013. Structural and geochronological constraints on the evolution of the eastern margin of the Tanzania Craton in the Mpwapwa area, central Tanzania. Precambrian Research 224, 671–689.
Thomas, R.J., Spencer, C., Bushi, A.M., Baglow, N., Boniface, N., Kock, G., Horstwood, M.S.A., Hollick, F., Jacobs, J., Kajara, S., Kamihanda, G., Key, R.M., Maganga, Z., Mbawala, F., McCourt, W., Momburi, P., Moses, F., Mruma, A., Myambilwa, Y., Roberts, N.M.W., Saidi, H., Nyanda, P., Khalid Nyoka, K., Millar, I., 2016. Geochronology of the central Tanzania Craton and its southern andeastern orogenic margins. Precambrian Research 277, 47–67.
Treloar, P.J., Kramers, J.D., 1989. Metamorphism and geochronology of granulites and migmatitic granulites from the Magondi Mobile Belt, Zimbabwe. Precambrian Research 45, 277–289.
Tsunogae, T., Dunkley, D.J., Horie, K., Endo, T., Miyamoto, T., Kato, M., 2014. Petrology and SHRIMP zircon geochronology of granulites from Vesleknausen, Lützow–Holm Complex, East Antarctica: Neoarchean magmatism and Neoproterozoic high-grade metamorphism. Geoscience Frontiers 5, 167–182.

Tsunogae, T., Yang, Q.Y., Santosh, M., 2015. Early Neoproterozoic arc magmatism in the Lützow–Holm Complex, East Antarctica: petrology, geochemistry, zircon U–Pb geochronology and Lu–Hf isotopes and tectonic implications. Precambrian Research 266, 467–489.

Tsunogae, T., Yang, Q.Y., Santosh, M., 2016. Neoarchean–Early Paleoproterozoic and Early Neoproterozoic arc magmatism in the Lützow–Holm Complex, East Antarctica: insights from petrology, geochemistry, zircon U–Pb geochronology and Lu–Hf isotopes. Lithos 263, 239–256.

Tsutsumi, Y., Horie, K., Sano, T., Miyawaki, R., Momma, K., Matsubara, S., Shigeoka, M., Yokoyama, K., 2012. LA-ICP-MS and SHRIMP ages of zircons in chevkinite and monazite tuffs from the Boso Peninsula, Central Japan. Bulletin of the National Museum of Nature and Science. Series C (Geology & Paleontology) 38, 15–32.

Unrug, R., 1983. The Lufilian Arc: a microplate in the pan-African collision zone of the Congo and the Kalahari Cratons. Precambrian Research 21, 181–196.

Vinyu, M.L., Hanson, R.E., Martin, M.W., Bowring, S.A., Jelsma, H.A., Krol, M.A., Dirks, P.H.G.M., 1999. U–Pb and $^{40}Ar/^{39}Ar$ geochronological constraints on the tectonic evolution of the easternmost part of the Zambezi orogenic belt, northeast Zimbabwe. Precambrian Research 98, 67–82.

White, R.W., Powell, R., Holland, T.J.B., Worley, B.A., 2000. The effect of TiO_2 and Fe_2O_3 on metapelitic assemblages at greenschist and amphibolite facies conditions: mineral equilibria calculations in the system K_2O–FeO–MgO–Al_2O_3–SiO_2–H_2O–TiO_2–Fe_2O_3. Journal of Metamorphic Geology 18, 497–511.

White, R.W., Powell, R., Clarke, G.L., 2002. The interpretation of reaction textures in Fe–rich metapelitic granulites of the Musgrave Block, central Australia: constraints from mineral equilibria calculations in the system K_2O–FeO–MgO–Al_2O_3–SiO_2–H_2O–TiO_2–Fe_2O_3. Journal of Metamorphic Geology 20, 41–55.

White, R.W., Powell, R., Holland, T.J.B., Johnson, T.E., Green, E.C.R., 2014. New mineral activity–composition relations for thermodynamic calculations in metapelitic systems. Journal of Metamorphic Geology 32, 261–286.

Williams, I.S., 1998. U–Th–Pb geochronology by ion microprobe. In: McKibben, M.A., Shanks, W.C. (Eds.), Applications of Microanalytical Techniques to Understanding Mineralizing Processes, Reviews in Economic Geology, vol. 7, pp. 1–35.

Williams, I.S., Claesson, S., 1987. Isotopic evidence for the Precambrian provenance and Caledonian metamorphism of high grade paragneisses from the Seve Nappes, Scandinavian Caledonides: II. Ion microprobe zircon U–Th–Pb. Contributions to Mineralogy and Petrology 97, 205–217.

Wilson, M., 1989. Igneous Petrogenesis: a Global Tectonic Approach. Unwin Hyman, London, p. 466 pp.

Wilson, J.F., Nesbitt, R.W., Fanning, C.M., 1995. Zircon geochronology of Archaean felsic sequences in the Zimbabwe craton: a revision of greenstone stratigraphy and a model for crustal growth. Geological Society, London, Special Publications 95, 109–126.

Winchester, J.A., Floyd, P.A., 1977. Geochemical discrimination of different magma series and their differentiation products using immobile elements. Chemical Geology 20, 325–343.